ISET Journal of Earthquake Technology, Paper No. 379, Vol. 35, No. 4, December 1998, pp. 113-141

EFFECT OF VISCOUS, VISCOPLASTIC AND FRICTION DAMPING ON THE RESPONSE OF SEISMIC ISOLATED STRUCTURES

Nicos Makris* and Shih-Po Chang**

*Associate Professor **Graduate Research Assistant
Department of Civil and Environmental Engineering,
SEMM, U. C. Berkeley, California, 94720, USA

ABSTRACT

In this paper the efficiency of various seismic isolation systems to protect structures from near-source ground motions is examined. It is first shown that under such motions the concept of equivalent linear damping has limited meaning since the transient response of a structure is more sensitive to the nature of the dissipation mechanism, rather than the amount of energy dissipated per cycle. Subsequently, physically realizable cycloidal pulses are introduced and their resemblance to recorded near-source ground motions is illustrated. The study uncovers the coherent component of some near-source acceleration records and their shaking potential of these records is examined. It is found that the response of structures with relatively low isolation periods is substantially affected by the high frequency fluctuations that override the long duration pulse, therefore the concept of seismic isolation is beneficial even for motions that contain a long duration pulse which generates the large recorded displacements and velocities. Furthermore, although cycloidal pulses can capture many characteristics of the displacement and velocity time histories recorded near the source, they are not dependable motions for structural response analysis. It is recommended that when available, near source records should be used and not their cycloidal approximation. Dissipation forces of friction (plastic) type are very efficient in reducing displacement demands although occasionally they are responsible for substantial base shears. The study concludes that a combination of relatively low viscous and friction dissipation forces is attractive since base displacements are substantially reduced without increasing appreciably base shears and superstructure accelerations.

KEYWORDS: Near-Source Ground Motions, Seismic Isolated Structures, Viscous Damping, Hysteretic Damping

INTRODUCTION

The dynamic response of a structure depends on its mechanical characteristics and the nature of the induced excitation. Mechanical properties which are efficient to mitigate the structure's response when subjected to certain inputs might have an undesirable effect during other inputs. Ground motions generated from earthquakes differ from one another in magnitude, source characteristics, distance and direction from the rupture location and local soil conditions. The ability of a structure to dissipate energy is central in controlling displacement demands, and various energy dissipation mechanisms have been proposed to enhance structural response (ATC, 1993). These energy dissipation mechanisms can be of various types such as viscous, rigid-plastic, elastoplastic, viscoplastic, or combination of them.

Under seismic excitations that have relatively long durations, a structure undergoes several cycles during the forced vibration part of the response; therefore, its response depends more on the amount of energy that is dissipated during each cycle (area under the force-displacement loop), rather than the nature of the dissipative force that develops (viscous-type, friction-type etc.). Because of this, the dissipation properties of structures are averaged over a cycle of motion and are expressed in term of dimensionless ratios which originate from the linear theory of structural dynamics.

During the last two decades, an ever increasing database of recorded ground motions demonstrated that the kinematic characteristics of ground motion near the fault of major earthquakes contain large displacement pulse from 0.5 m to more than 1.5 m with peak velocities of 0.5 m/s or higher. In some cases the coherent pulse is distinguishable not only in the displacement and velocity histories but also in the acceleration history which happens to be a rather smooth signal. In other cases acceleration histories recorded near the source contain high-frequency spikes and resemble the traditional random-like signal;

however, their velocity and displacement histories uncover a coherent long-period pulse with some high frequency fluctuations that override along (Campillo et al. 1989, Iwan and Chen 1994).

The challenge in seismic protection with such motions is the selection of mechanical properties that will improve the response of a structure that experiences the high frequency spike and the low-frequency, low-acceleration pulse. Previous studies (Anderson and Bertero 1986, Hall et al. 1995, Iwan 1997) indicated that what make near-source ground motions particularly destructive to some structures is not their peak ground acceleration but their long duration pulse which represents the incremental velocity that the above ground mass has to reach. These indications challenged the concept of seismic isolation. This paper addresses this challenge in a systematic way showing that under near-source ground motions seismic isolation is effective provided that the appropriate energy dissipation mechanism is provided.

In this study, the effect of various dissipation mechanisms in reducing the response of seismically isolated structure subjected to near-source ground motions is examined in detail. It is first shown through a comprehensive study that during pulse-type ground motions the concept of equivalent linear damping is no longer valid because the response is strongly transient. The response of the structure is much more sensitive to the nature of the dissipation mechanism, rather than to the amount of energy dissipated per cycle. Accordingly, damping ratio quantities that are used in design such as the effective damping coefficient, β_{eff}, should be used with caution. Subsequently, selected near-source ground motions are presented and their resemblance to physically realizable cycloidal pulses is shown. A type-A cycloidal pulse approximates a forward motion; a type-B cycloid pulse approximates a forward-and-back motion; whereas, a type-C_n pulse approximates a recorded motion that exhibits n main pulses in its displacement history. The velocity histories of all type-A, type-B and type-C_n pulses are differentiable signals that result in finite acceleration values.

While the proposed cycloidal pulses capture many of the kinematic characteristics of the displacement and velocity histories of recorded near-source ground motions, in most cases the resulting accelerations are poor predictions of the recorded histories. This is because in many near-source ground motions there are high frequency fluctuations that override the long duration pulse. It is shown that the response of structures with relatively low isolation periods is affected significantly by these high frequency fluctuations indicating that the concept of seismic protection by lengthening the isolation period is beneficial when the appropriate type of energy dissipation is provided. The paper concludes that a combination of relatively low values of friction and viscous damping results in an attractive design since displacements are substantially reduced without increasing appreciably base shears and superstructure accelerations.

MODAL DAMPING RATIO AND EFFECTIVE DAMPING COEFFICIENT

In order to represent the ability of a structure or a structural component to dissipate energy, various dimensionless quantities have been proposed to express damping. This section reviews the definitions and relations of the two most widely used ratios, that of the modal damping ratio, ξ_i, and that of the effective damping coefficient, β_{eff}.

For a 1-DOF linear oscillator with mass, m, stiffness, $K = m\omega_0^2$ and viscous damping, C, the viscous damping ratio is defined as $\xi = C/2m\omega_0$. Since for a 1-DOF there is only one mode, the first modal damping, $\xi_1 = \xi$. Clearly, the modal damping (viscous damping ratio) has meaning only when the structural system has finite inertial mass ($m \neq 0$).

During a steady-state harmonic motion with amplitude U_0 and frequency Ω, the damping constant, C, is related to the energy dissipated per cycle, W_D, with

$$C = 2\xi\, m\omega_0 = \frac{W_D}{\pi\, \Omega U_0^2} \tag{1}$$

where W_D is the area under the steady-state force-displacement loop. Recognizing that the maximum strain energy stored in the oscillation during this motion is $E_s = \frac{1}{2} m\omega_0^2 U_0^2$, the damping coefficient ξ is

$$\xi = \frac{1}{4\pi} \frac{\omega_0}{\Omega} \frac{W_D}{E_S} \tag{2}$$

When the frequency of vibration of the 1-DOF system happens to be the natural frequency of the oscillator (resonance), then the modal damping, $\xi = W_D/(4\pi E_S)$, which is the familiar expression presented in most books of structural and soil dynamics (Chopra 1995, Kramer 1996).

With the development of seismic protection systems and energy dissipation devices, structural engineers faced the need to quantify the energy dissipation capabilities of isolation components with virtually no inertial mass (during component testing, the inertia forces recorded by the load cell are very small compared to the forces originating from elasticity and dissipation). The most popular way to quantify energy dissipation of a protective device is to impose a cyclic displacement $U(t) = U_0 \sin \Omega t$ on the device and measure the resulting force that develops. During such tests, the energy dissipated per cycle is the area under the force displacement loop and the effective damping coefficient β_{eff} of the protective device is defined as

$$\beta_{eff} = \frac{1}{2\pi} \frac{W_D}{K_I U_0^2} \tag{3}$$

where K_I is the effective stiffness of the isolation device.

Consider now the 1-DOF system shown on Figure 1 (top) that consists of a rigid block with mass m supported on an isolation system with effective stiffness $K_I = m\omega_I^2$. For this structural system, the combination of (2) and (3) gives

$$\xi = \xi_1 = \frac{\omega_I}{\Omega} \beta_{eff} \tag{4}$$

where $\omega_I = \sqrt{K_I / m}$ and Ω is the frequency at which the superstructure oscillates. Equation (4) relates the modal damping of a structural system with finite mass to the effective damping coefficient, β_{eff}, of an isolation system with virtually no mass. In many occasions during earthquake shaking, the superstructure oscillates near its natural frequency $(\Omega \approx \omega_I)$, and because of Equation (4) it has become a practice to assume $\xi \approx \beta_{eff}$. However, as it will be shown in this paper under pulse-type motions despite the fact that structures oscillate at their natural frequencies, $\xi \neq \beta_{eff}$.

Consider now the 2-DOF base isolated structure shown on Figure 1 (bottom). The isolation frequency of the structure is $\omega_I = \sqrt{K_I/(m_b + m)}$ where K_I is again the effective stiffness of the isolation system. The natural frequency of the fixed base superstructure is $\omega_s = \sqrt{K_s / m}$. Furthermore, the isolation damping is defined as $C_I = 2\xi_I (m_b + m)\omega_I$ and the superstructure damping is defined as $C_s = 2\xi_s m\omega_s$. The 2-DOF structure shown on Figure 1 (bottom) has two modes and the modal frequencies and modal damping ratios are given by (Kelly 1997)

$$\omega_1 = \omega_I \sqrt{1 - \gamma \frac{\omega_I^2}{\omega_s^2}} \qquad \xi_1 = \xi_I \left(1 - \frac{3}{2} \gamma \frac{\omega_I^2}{\omega_s^2}\right) \tag{5}$$

$$\omega_2 = \frac{\omega_s}{\sqrt{1-\gamma}} \sqrt{1 + \gamma \frac{\omega_I^2}{\omega_s^2}} \qquad \xi_2 = \frac{1}{\sqrt{1-\gamma}} \left(\xi_s + \xi_I \gamma \frac{\omega_I^2}{\omega_s^2}\right)\left(1 - \frac{1}{2} \gamma \frac{\omega_I^2}{\omega_s^2}\right) \tag{6}$$

where $\gamma = m/(m + m_b)$. Because of the presence of the isolation system, the participation of the first mode is dominant and the 2-DOF structure will primarily oscillate along its first mode. Accordingly,

$$\xi_1 = \frac{1}{4\pi}\frac{W_D(\omega_1)}{E_S} = \beta_{eff}(\omega_1) \approx \xi_1 \tag{7}$$

Since the effective damping coefficient of most isolation systems is nearly frequency independent, it has now become a practice to assume that $\xi_1 = \xi_1 = \beta_{eff}$. This relation also is no longer valid during pulse-type excitations.

CLOSED FORM APPROXIMATION OF NEAR-SOURCE GROUND MOTIONS

Figure 2 (left) shows the East-West component of the acceleration, velocity and displacement histories of the September 19th, 1985 Michoacan earthquake recorded at the Caleta de Campos station (Anderson et al. 1986). The motion resulted in a forward displacement of the order of 0.4 m. The coherent long duration pulse responsible for most of this displacement can be also distinguished in the velocity history; whereas, the acceleration history is crowded with high frequency spikes. Figure 2 (right) plots the acceleration, velocity and displacement histories of type- A cycloidal pulse given by (Jacobsen and Ayre 1958, Makris 1997).

$$\ddot{u}_g(t) = \omega_p \frac{v_p}{2}\sin(\omega_p t) \qquad 0 \le t \le T_p \tag{8}$$

$$\dot{u}_g(t) = \frac{v_p}{2} - \frac{v_p}{2}\cos(\omega_p t) \qquad 0 \le t \le T_p \tag{9}$$

$$u_g(t) = \frac{v_p}{2}t - \frac{v_p}{2\omega_p}\sin(\omega_p t) \qquad 0 \le t \le T_p \tag{10}$$

In constructing Figure 2 (right), the values of T_p = 5.0 s and v_p = 0.16 m/s were used which are approximations of the duration and velocity amplitude of the main pulse. Figure 2 indicates that a simple one-sine pulse can capture some of the kinematic characteristics of the motion recorded at the Caleta de Campos station. On the other hand, the resulting acceleration amplitude $a_p = \omega_p v_p/2 \approx 0.01$ g, is one order of magnitude smaller than the recorded peak ground acceleration.

Another example of a recorded ground motion that resulted in a forward pulse is the fault parallel motion recorded at the Lucerne Valley station during the June 18th, 1992 Landers earthquake which is shown in Figure 3 (left). Although the displacement history results in a clean forward pulse, the acceleration history is crowded with high-frequency spikes that reach 0.75 g. On the right of Figure 3, the results of Equations (8) to (10) are shown for the values of T_p = 7.0 s and v_p = 0.5 m/s which are approximations of the pulse period and the pulse velocity amplitude of the recorded motion. Again, while the resulting displacement history is in very good agreement with the record, the resulting acceleration amplitude $a_p = \omega_p v_p/2 \approx 0.045$ g is one order of magnitude smaller than the recorded peak ground acceleration.

Figure 4 (left) shows the acceleration, velocity and displacement histories of the fault-normal motions recorded at the El Centro Station, array #5 during the October 15th, 1979 Imperial Valley earthquake. This motion resulted in a forward-and-back pulse with a 3.2 s duration. In this case the coherent long period pulse is distinguishable not only in the displacement and velocity record, but also in the acceleration record. Figure 4 (right) plots the acceleration, velocity and displacement histories of a type- B cycloidal pulse given by Makris (1997)

$$\ddot{u}_g(t) = \omega_p v_p \cos(\omega_p t) \qquad 0 \le t \le T_p \tag{11}$$

$$\dot{u}_g(t) = v_p \sin(\omega_p t) \qquad 0 \le t \le T_p \tag{12}$$

$$u_g(t) = \frac{v_p}{\omega_p} - \frac{v_p}{\omega_p}\cos(\omega_p t) \qquad 0 \le t \le T_p \tag{13}$$

In constructing Figure 4 (right) the values of T_p = 3.2 s and v_p = 0.7 m/s were used as approximate values of the pulse period and velocity amplitude of the recorded motions shown on Figure 4 (left).

Figure 5 (left) portrays the fault-normal components of the acceleration, velocity and displacement histories of the January 17th, 1994 Northridge earthquake recorded at the Rinaldi station. This motion resulted in a forward ground displacement that recovered partially. The velocity history has a large positive pulse and a small negative pulse that is responsible for the partial recovery of the ground displacement. Had the negative velocity pulse generated the same area as the positive velocity pulse, the ground displacement would have fully recovered. Accordingly, the fault normal component of the Rinaldi station record is in-between a forward and a forward-and-back pulse. Figure 5 (center) shows the results of Equations (8) to (10) by assuming a pulse duration T_p = 0.8 s and a velocity amplitude v_p = 1.75 m/s which are approximations of the duration and velocity amplitude of the first main pulse shown on the record. Figure 5 (right) shows the results of Equations (11) to (13) by considering a pulse duration T_p =1.3 s and a velocity amplitude v_p = 1.3 m/s. A similar situation prevails for the fault normal motion recorded at the Lucerne Valley station during the June 18th, 1992 Landers earthquake which is shown on Figure 6 (left). Again, the velocity history has a large negative pulse that is followed by a smaller positive pulse. Had the second positive pulse generated the same area as the negative pulse, the ground displacement would have fully recovered. Figure 6 (center) shows the results of Equations (8) to (10) by considering a pulse duration T_p = 3.0 s and a velocity amplitude v_p = 1.0 m/s which are approximations of the duration and velocity amplitude of the first main pulse shown on the record. Figure 6 (right) shows the results of Equations (11) to (13) by considering a pulse duration T_p = 5.0 s and a velocity amplitude of v_p = 1.0 m/s. Trends similar to those observed in Figure 5 are also present in Figure 6. Although the constructed displacement and velocity histories either with a type-A pulse or a type-B pulse are capturing distinct elements of the kinematics of the recorded motion, the resulting ground acceleration is an order of magnitude smaller than the peak recorded value.

Not all near source records are forward, or forward-and-back pulses. Figure 7 (left) portrays the fault-normal component of the acceleration, velocity and displacement time histories recorded at the Sylmar station during the January 17th, 1994 Northridge earthquake. The ground displacement consists of two main long-period cycles, the first cycle being the largest and the subsequent ones decaying. These long period pulses are also distinguishable in the ground velocity history where the amplitude of the positive pulses is larger than the amplitude of the negative pulses. Near-fault ground motions, where the displacement history exhibits one or more long duration cycles, are approximated with type-C pulses. A n-cycle ground displacement is approximated with a type-C_n pulse that is defined as

$$\ddot{u}_g(t) = \omega_p v_p \cos(\omega_p t + \varphi) \qquad 0 \le t \le \left(n + \frac{1}{2} - \frac{\varphi}{\pi}\right) T_p \qquad (14)$$

$$\dot{u}_g(t) = v_p \sin(\omega_p t + \varphi) - v_p \sin(\varphi) \qquad 0 \le t \le \left(n + \frac{1}{2} - \frac{\varphi}{\pi}\right) T_p \qquad (15)$$

$$u_g(t) = -\frac{v_p}{\omega_p}\cos(\omega_p t + \varphi) - v_p t \sin(\varphi) + \frac{v_p}{\omega_p}\cos(\varphi) \qquad 0 \le t \le \left(n + \frac{1}{2} - \frac{\varphi}{\pi}\right) T_p \qquad (16)$$

In deriving these expressions, it was required that the displacement and velocity are differentiable signals. The value of the phase angle, φ, is determined by requiring that the ground displacement at the end of the pulse is zero. A type-C_n pulse with frequency $\omega_p = 2\pi/T_p$ has duration $T = (n+1/2)T_p - 2\varphi/\omega_p = (n+1/2-\varphi/\pi)T_p$. In order to have a zero ground displacement at the end of a type-C_n pulse

$$\int_0^{(n+1/2-\varphi/\pi)T_p} \dot{u}_g(t)\, dt = 0 \qquad (17)$$

Equation (17) after evaluating the integral gives

$$\cos[(2n+1)\pi-\varphi]+[(2n+1)\pi-2\varphi]\sin\varphi-\cos\varphi=0 \tag{18}$$

The solution of the transcendental equation given by Equation (18) gives the value of the phase angle φ. As an example for a type-C_1 pulse $(n=1)$, $\varphi=0.0697\pi$; whereas, for a type-C_2 pulse $(n=2)$, $\varphi=0.0410\pi$. Figure 8 (third and fourth column) plots the acceleration, velocity and displacement histories of a type-C_1 and a type-C_2 pulse.

As n increases, a type-C_n pulse tends to a harmonic steady-state excitation. Figure 8 summarizes the acceleration, velocity and displacement shapes of a forward-pulse, a forward-and-back pulse, a type-C_1 and a type-C_2 pulse. The displacement of a forward-and-back pulse has the same shape as the velocity of a forward pulse. Similarly, the displacement of a type-C_1 pulse resembles the shape of the velocity of a forward-and-back pulse and the shape of the acceleration of a forward pulse. This shows that type-C pulses provide a continuous transition from cycloidal pulses to harmonic steady-state motions.

MODELING OF THE DISSIPATION MECHANISMS OF PRACTICAL ISOLATION SYSTEMS

In addition to its restoring capability, an isolation system dissipates energy. The dissipation mechanism of practical isolation systems can be approximated with various macroscopic models: (a) Viscous model (high damping rubber bearings, elastomeric bearings and viscous fluid dampers); (b) rigid-plastic model (sliding bearings); (c) elastic-plastic model (lead rubber bearings); (d) viscoplastic model (sliding bearings and viscous fluid dampers, elastomeric bearings and friction dampers, elastomeric bearings and controllable fluid dampers, sliding bearing and controllable fluid dampers); (e) elastoviscoplastic model (lead rubber bearings and viscous dampers).

Figure 9 shows the force-displacement loops of these five dissipation mechanisms. It is worth mentioning that case 2 is the limiting case of 3 where the yield displacement becomes very small; whereas, case 2 is also the limiting case of 4 where the viscous component vanishes. The elastoviscoplastic case 5 is the most general case and the dissipation force can be expressed mathematically with:

$$P(t)=C_I\dot{u}_b(t)+K_I u_y z(t) \tag{19}$$

where u_b is the base displacement shown on Figure 1 (bottom), K_I is some reference stiffness, u_y is the value of the yield displacement of the isolation system and z is a hysteretic dimensionless quantity that is governed by the following equation:

$$u_y\dot{z}+\gamma\,|\dot{u}_b(t)|\,z\,|z|^{n-1}+\beta\,\dot{u}_b(t)\,|z|^n-A\dot{u}_b(t)=0 \tag{20}$$

The model given by Equations (19) and (20) is a special case of the Bouc-Wen model (Wen 1975, 1976) enhanced with a viscous term. In Equation (20), β, γ, n and A are dimensionless quantities that control the shape of the hysteretic loop. It can be shown that when $A=1$, parameter K_I in Equation (19) becomes the pre-yielding elastic stiffness. As an example in a lead rubber bearing, K_I is the stiffness of the lead core before yielding. Based on this observations parameter, A, is set equal to one. C_I is the viscous damping coefficient of the isolation system $C_I=C_b+C_d$ where, $C_b=2\xi_b(m+m_b)\omega_I$, is the viscous damping originating from the elastomeric bearings and $C_d=2\xi_d(m+m_b)\omega_I$ is the viscous damping originating from possible additional damping devices.

For the special case of rigid viscoplastic behavior, the yield displacement $u_y\to 0$ and the pre-yielding stiffness $K_e\to\infty$ so that the product, $u_y K_e\to P_y$, is a finite yield force. Under these conditions, Equation (19) reduces to the Bingham model of viscoplasticity.

$$P(t)=C_I\dot{u}_b(t)+P_y\,\mathrm{sgn}[\dot{u}_b(t)] \tag{21}$$

in which $P_y = P_{by} + P_{dy}$, where $P_{by} = \mu(m + m_b)g$ is the yield (friction type) force originating from the sliding bearing and P_{dy} is the yield force that might originate from additional damping devices such as controllable fluid dampers. In this paper, the friction force is represented with the general formulation given by Equations (19) and (20) where the yield displacement is assumed very small $(u_y \approx 0.2\,\text{mm})$. This value is of the order of the yield value of the teflon interface in sliding bearings (Mokha et al. 1988).

With reference to Figure 1b, the equation of motion of the 2-DOF structure is (Kelly 1997):

$$\begin{bmatrix} 1 & \gamma_m \\ 1 & 1 \end{bmatrix}\begin{bmatrix} \ddot{u}_b(t) \\ \ddot{u}_s(t) \end{bmatrix} + \begin{bmatrix} 0 & 0 \\ 0 & 2\xi_s\omega_s \end{bmatrix}\begin{bmatrix} \dot{u}_b(t) \\ \dot{u}_s(t) \end{bmatrix} + \begin{bmatrix} \omega_b^2 & 0 \\ 0 & \omega_s^2 \end{bmatrix}\begin{bmatrix} u_b(t) \\ u_s(t) \end{bmatrix} + \begin{bmatrix} 1 \\ 0 \end{bmatrix}\alpha(t) = -\begin{bmatrix} 1 \\ 1 \end{bmatrix}\ddot{u}_g(t) \qquad (22)$$

where $\gamma_m = m_s/(m + m_b)$ and $\alpha(t) = P(t)/(m + m_b)$ in which $P(t)$ is the dissipation force given by Equation (19) or (21). The parametric analysis presented in this paper is conducted by solving Equation (22) for various representations of the dissipative force $P(t)$.

The response of the 2-DOF structure shown on Figure 1 (bottom) which is expressed with Equation (22) is computed using a state-space formulation where the state vector of the system is $y(t) = \langle u_b(t) \quad \dot{u}_b(t) \quad u_s(t) \quad \dot{u}_s(t) \quad z(t) \rangle^T$. The seismic response of isolated overpasses like the one shown in Figure 10 is computed by setting the natural frequency of the superstructure very large.

PARAMETRIC STUDY

The formulation presented in the previous section is first used to predict the response of a 1-DOF overcrossing shown in Figure 10. Figure 10 (top) depicts an overcrossing that is isolated at the center bent and end-abutments; whereas, Figure 10 (bottom) depicts an overcrossing that is rigidly connected to its center bent and supported on isolation bearings at the end-abutments. Typical values of isolation periods range from T_I = 2 s or more for the top configuration, down to T_I = 1 s or even less for the bottom configuration.

The first column of Figure 11 shows the response of a 1-DOF with isolation period, T_I = 2 s and viscous isolation damping ξ_I = 15% when subjected to the type-A cycloidal front with T_p = 1.0 s and the Rinaldi station record shown on Figure 5. For the type-A pulse (first and second row), relative displacements reach 50 cm (20 in); whereas the base shear coefficient exceeds the value of 0.5. The second column on Figure 11 plots the response of the isolated structure where the isolation damping has been doubled by adding viscous dampers, $\xi_I = \xi_b + \xi_d = 30\%$. With a total isolation damping coefficient of $\xi_I = 30\%$ the base displacement reduces by 30 % (35 cm) and the base shear reduces by 15 %. The reason that under the presence of twice the viscous damping the base shear reduces is that, although additional damping increases the damping forces, it decreases displacements resulting to smaller elastic forces.

We are now interested in computing the effective damping coefficient of the 1-DOF structure during this shaking. Under a pulse excitation with duration smaller than the natural period of a structure, its vibration period is very close to its natural period. Indeed, the top graphs of all columns of Figure 11 clearly show that the 1-DOF completes a cycle within 2 s = T_I. Consequently, $\Omega = \omega_I$, and according to Equation (4) the effective damping coefficient should be $\beta_{eff} = \xi_I = 15\%$ for the response shown on the first column, and $\beta_{eff} = \xi_I = 30\%$ for the response shown in the second column. The area of the loops shown in the second row is equal to $\overline{W}_D = W_D/(mg)$ and Equation (3) allows for a direct measurement of the resulting effective damping coefficient, which is given by

$$\beta_{eff} \approx \frac{1}{2\pi}\frac{\overline{W}_D g}{\omega_I^2 D^2} \qquad (23)$$

where $D = (|u_{min}| + |u_{max}|)/2$. Equation (23) gives a value of $\beta_{eff} \approx 0.20$ for the response shown on the first column, and a value of $\beta_{eff} \approx 0.37$ for the response shown on the second column. These values are 30 % and 20 % larger than the corresponding values obtained with Equation (4). The reason for this discrepancy is that the definitions of ξ and β_{eff} given by Equations (2) and (3) are for harmonic-steady-state vibrations and not for transient motions, like those shown at the top of Figure 11.

The third column on Figure 11 plots the response of the isolated structure where the isolation damping is only of friction type (rigid-plastic damping). It is shown that for this system ($T_I = 2\,s$), a coefficient of friction, $\mu = 18\,\%$, is needed to achieve the same displacement reduction as 30 % viscous coefficient achieves. When the dissipation is due to friction only (rigid-plastic), $P(t) = \mu\ mg\ \mathrm{sgn}[\dot{u}_b(t)]$, Equation (3) simplifies to

$$\beta_{eff} \approx \frac{2\mu g}{\pi\omega_I^2 D} = \frac{2\alpha_y}{\pi\omega_I^2 D} \tag{24}$$

For the loop shown in the third column of Figure 11, Equation (24) gives $\beta_{eff} = 38\,\%$ which is approximately the same amount of effective damping coefficient as from the viscously-damped structure. The last column on Figure 11 plots the response of the isolated structure that combines viscous damping, $\xi_I = 15\,\%$, and friction damping that corresponds to $\mu = 9\,\%$. This combination of viscous and friction damping achieves the same displacement reduction that was achieved with the other two configurations. Furthermore, Equation (23) results into an effective damping coefficient, $\beta_{eff} = 38\,\%$, which is comparable with the values of β_{eff} that resulted from the two other systems.

Figure 11 (bottom) shows the response of the same 1-DOF structure with $T_I = 2\,s$ when excited by the Rinaldi station record. With viscous isolation damping $\xi_I = 15\,\%$ the maximum displacement is 44 cm, which is 17 % less than the maximum displacement reached under a type-A pulse front with nearly the same velocity pulse. The increase of the isolation damping from $\xi_I = 15\,\%$ to $\xi_I = 30\,\%$ reduced the response from 44 cm to 32.4 cm – a 30 % reduction which is the same amount of reduction that is achieved in the case of a pulse type-A motion.

The third column on Figure 11 plots the response of the 1-DOF structure under rigid-plastic dissipation ($\mu = 18\,\%$). It is interesting to note that the maximum displacement is 37.4 cm, which is more than the displacement that was reached under a pulse type A motion (see first row on Figure 11), although now the resulting $\beta_{eff} = 42\,\%$. Furthermore, the value of $\mu = 18\,\%$ now results in a 5 cm larger displacement response and a 20 % larger base shear than the response obtained with $\xi_I = 30\,\%$. Consequently, this example shows that two systems which are equivalent under one input exhibit opposite trends under a different but similar input and that the concept of effective damping coefficient has little meaning since its value is strongly response-dependent.

The seismic performance of the rigid block equipped with various types of damping mechanisms in its isolation system is summarized on Figure 12, where displacement and base shear spectra are plotted due to the fault normal component of the Rinaldi station record (left), a type-A pulse excitation with $T_p^A = 0.8\,s$ (center) and a type-B pulse excitation with $T_p^B = 1.3\,s$ (right) and kinematic characteristics that approximate those of the Rinaldi station record. It is observed that at the low isolation period range (say $T_I < 2.0\,s$) additional viscous damping reduces the displacements and base shears in the most effective way. Friction dissipation alone ($\xi_I = 0$, $\mu = 18\,\%$) becomes effective in reducing displacements at large isolation periods; however, the resulting base shears are the largest. A combination of viscous and friction damping results into an attractive performance since the effective reduction of displacements is accompanied with base shear that are lower than those resulting form friction dissipation alone. As an example Figure 13 (left) indicated that an isolation period $T_I = 3.0\,s$ with $\xi_I = 15\,\%$ and $\mu = 9\,\%$ will result in a base displacement of $u_b = 33\,cm$ and a base shear

coefficient of 0.25. On the other hand additional energy dissipation devices that will increase the damping of a 1 s period structure from 5 % to 30 % will reduce displacements to half; whereas the base shears will exceed the weight of the structure. Another interesting observation is that the response spectra of the fault normal component of the Rinaldi station record has a smooth shape, resembling the shape of the spectra obtained with the pulse type-A and pulse type-B excitations.

Figure 13 plots the displacement and base shear spectra of the fault normal component of Lucerne Valley record (left), a type-A pulse with $T_p^A = 3\,\text{s}$ (center) and a type-B pulse with $T_p^B = 5\,\text{s}$ (right). In this case friction dissipation alone results into the smallest displacement values; whereas, the combination of viscous and friction damping results into the smallest base-shear values. In the low range of isolation periods ($T_I < 2.0\,\text{s}$) the spectrum from the recorded motion is substantially different from the spectrum resulting from the pulse motions, indicating that in the low isolation period range the response is governed by the high frequency fluctuations that override the long duration pulse. At the high range of isolation periods ($T_I > 2.0\,\text{s}$) viscous dissipation results into large displacements which are reduced substantially when some friction dissipation is introduced. Again, a 3 s isolation period with $\xi_I = 15$ % and $\mu = 9$ % results to an attractive design.

Figures 14 and 15 illustrate the effects of the high frequency fluctuations that override the long duration pulse. Under the Caleta de Campos and the Lucerne Valley forward motions, the base shear that develops in the long period structures when friction dissipation is included, is larger than the base shear resulting from viscous dissipation. In contrast, when only the long duration pulse is considered alone (right graphs), the trend is reversed. Figures 14 and 15 show clearly that although cycloidal pulses capture many characteristics of the displacement and velocity time histories recorded near the source, they are not dependable motions for structural response analysis since the high frequency fluctuations influence drastically the response.

Figure 16 plots the displacement and base shear spectra of the fault normal component of the El Centro Array #5 record (left) and a type-B pulse with $T_p^B = 3.2\,\text{s}$ (right). In this case, viscous dissipation results not only to large displacement but also to substantial base shear. Friction dissipation eliminates amplification due to resonance for isolation periods longer than 2 s. A 3 s isolation period with $\xi_I = 15$ % and $\mu = 9$ % results again to an attractive response. Figure 17 shows that dissipation forces of friction type are very efficient to reduce displacements and base shears even when the isolation period is in the vicinity of the predominant period of the long period pulse ($T_p = 2.3\,\text{s}$).

This parametric study on the response of 1-DOF structure indicates that in general the combination of viscous and friction forces is effective in reducing displacements by keeping the base shears at low levels.

We now investigate the effect of viscous, viscoplastic and rigid-plastic dissipation mechanisms on the response of the 2-DOF structure shown on Figure 1 (bottom). As an example, Figure 18 plots the base displacement, base shear, superstructure drift and total acceleration time histories of the superstructure of a 2-DOF system equipped with the dissipation mechanisms introduced in the previous section. The isolation period is $T_I = 2.0\,\text{s}$ and the superstructure period is $T_s = 0.25\,\text{s}$. The response of the base of the 2-DOF structure when subjected to the Rinaldi station record is very close to the response of 1-DOF with the same isolation period ($T_I = 2.0\,\text{s}$) shown on Figure 11 bottom. It is interesting to note that by increasing the viscous damping from 15 % to 30 % the base displacement decreased from 43.7 cm to 32.2 cm (30 %) whereas the increase of interstory drift was less than 1 % and the increase in the superstructure acceleration was less than 2 %, which shows that in this case additional damping decreased substantially base displacement without affecting interstory drifts and superstructure accelerations. When however friction damping is used ($\mu = 18\,\%$) the displacements are reduced only to 37.3 cm (16 %), whereas interstory drift and superstructure acceleration have increased by 45%. The combination of viscous ($\xi_I = 15\,\%$) and hysteretic dissipation ($\mu = 9\,\%$) reduced the base displacements to 34.6 cm (23 % reduction), whereas interstory drift increased by 27 % and superstructure acceleration have increased by 30 %.

The seismic performance of the 2-DOF isolated structure equipped with various type of damping mechanisms in its isolation system is summarized on Figure 19 where displacement, base shear, interstory

drift and superstructure acceleration spectra are plotted due to the fault normal component of the Rinaldi station record (left), a type-A pulse excitation with $T_p^A = 0.8\,\mathrm{s}$ (center) and a type-B pulse excitation with $T_p^B = 1.3\,\mathrm{s}$ (right). In this case, supplemental energy dissipation with viscous damping outperforms all other dissipation mechanisms. In contrast, Figure 20 shows that under the Sylmar motion of the Northridge earthquake an isolation system with $T_I = 3\,\mathrm{s}$ and a combination of viscous damping $\xi_I = 15\,\%$ and friction damping $\mu = 9\,\%$ results to the most attractive response.

CONCLUSIONS

The efficiency of various dissipative mechanisms to protect structures from pulse-type and near-source ground motion has been investigated in detail. It was first shown that under these motions the concept of equivalent linear damping has limited meaning since the transient response of a structure is more sensitive to the nature of the dissipation forces, rather than the amount of energy dissipated per cycle.

Physically realizable trigonometric pulses have been introduced and their resemblance to selected near-source ground motions was illustrated. It is found that structural response quantities due to the recorded motions resemble the structural response quantities due to trigonometric pulse type motions only when the isolation period reaches high values (say $T_I = 3\,\mathrm{s}$ or more). The response of structures with relatively low isolation periods (say $T_I < 2\,\mathrm{s}$) is substantially affected by the high frequency motion that overrides the long duration pulse; therefore the concept of seismic isolation is beneficial even for motions that contain long velocity and displacement pulses. The study concludes that for isolated structures with isolation period $T_I \approx 3.0\,\mathrm{s}$ a combination of viscous and friction dissipation forces is attractive since displacements are substantially reduced without appreciably increasing base shears and superstructure accelerations. The presence of friction (plastic) forces removes any resonant effect that a long-duration pulse has on a long-period isolation system.

ACKNOWLEDGEMENTS

Partial financial support for this study was provided by the National Science Foundation under Grant CMS-9696241 and the California Department of Transportation under Grant RTA59A169.

REFERENCES

1. Anderson, J.C. and Bertero, V. (1986). "Uncertainties in Establishing Design Earthquakes," Journal of Struct. Eng., ASCE, Vol. 113, pp. 1709-1724.
2. Anderson, J.G., Bodin, P., Brune, J.N., Prince, J. and Singh, S. K. (1986). "Quaas R. & Onate M., Strong Ground Motion from the Michoacan, Mexico Earthquake," Science, Vol. 233, pp. 1043-1049.
3. ATC-17-1 (1993). Proceedings of Seminar on Seismic Isolation, Passive Energy Dissipation, and Active Control, Vol. 1 & 2, Applied Technology Council.
4. Campillo, M., Gariel, J. C., Aki, K. and Sanchez-Sesma, F. J. (1989). "Destructive Strong Ground Motions in Mexico City: Source, Path, and Site Effects during Great 1985 Michoagan Earthquake," Bulletin Seismological Soc. of America, Vol. 79, No. 6, pp. 1718-1735.
5. Chopra, A.K. (1995). "Dynamics of Structures, Theory and Applications to Earthquake engineering," Prentice Hall, New Jersey.
6. Hall, J. F., Heaton, T. H., Halling, M. W. and Wald, D. J. (1995). "Near-Source Ground Motions and its Effects on Flexible Buildings," Earthquake Spectra, Vol. 11, pp. 569-605.
7. Iwan W. D. (1997). "Drift Spectrum: Measure of Demand for Earthquake Ground Motions," Journal of Structural Engineering, Vol. 123, No. 4, pp. 397-404.
8. Iwan, W.D. and Chen, X.D. (1994). "Important Mear-Field Ground Motion Data from the Landers Earthquake," Proc. 10th European Conf. Earthquake Engrg, Vienna.
9. Jacobsen, L.S. and Ayre, R.S. (1958). "Engineering Vibrations," McGraw-Hill, New York, NY.

10. Kelly, J.M. (1997). "Earthquake Resistant Design with Rubber," Springer-Verlag, London.
11. Kramer, S.L. (1996). "Geotechnical Earthquake Engineering," Prentice Hall, New Jersey.
12. Makris, N. (1997). "Rigidity-Plasticity-Viscosity: Can Electrorheological Dampers Protect Base-Isolated Structures from Near-Source Ground Motions ?" Earthquake Engineering and Structural Dynamics, Vol. 26, pp. 571-591.
13. Mokha, A., Constantinou, M.C. and Reinhorn, A.M. (1988). "Teflon Bearings in Aseismic Baselisolation: Experimental Studies and Mathematical Modeling," Technical Report NCEER-88-0038, SUNY Buffalo.
14. Uniform Building Code (1994), International Conference of Building Officials, Whittier, CA.
15. Wen, Y.K. (1975). "Approximate Method for Nonlinear Random Vibration," Journal of the Engineering Mechanics Division, ASCE, Vol. 101, No. EM4, pp. 389-401.
16. Wen, Y.K. (1976). "Method for Random Vibration of Hysteretic Systems," Journal of the Engineering Mechanics Division, ASCE, Vol. 102, No. EM2, pp. 249-263.

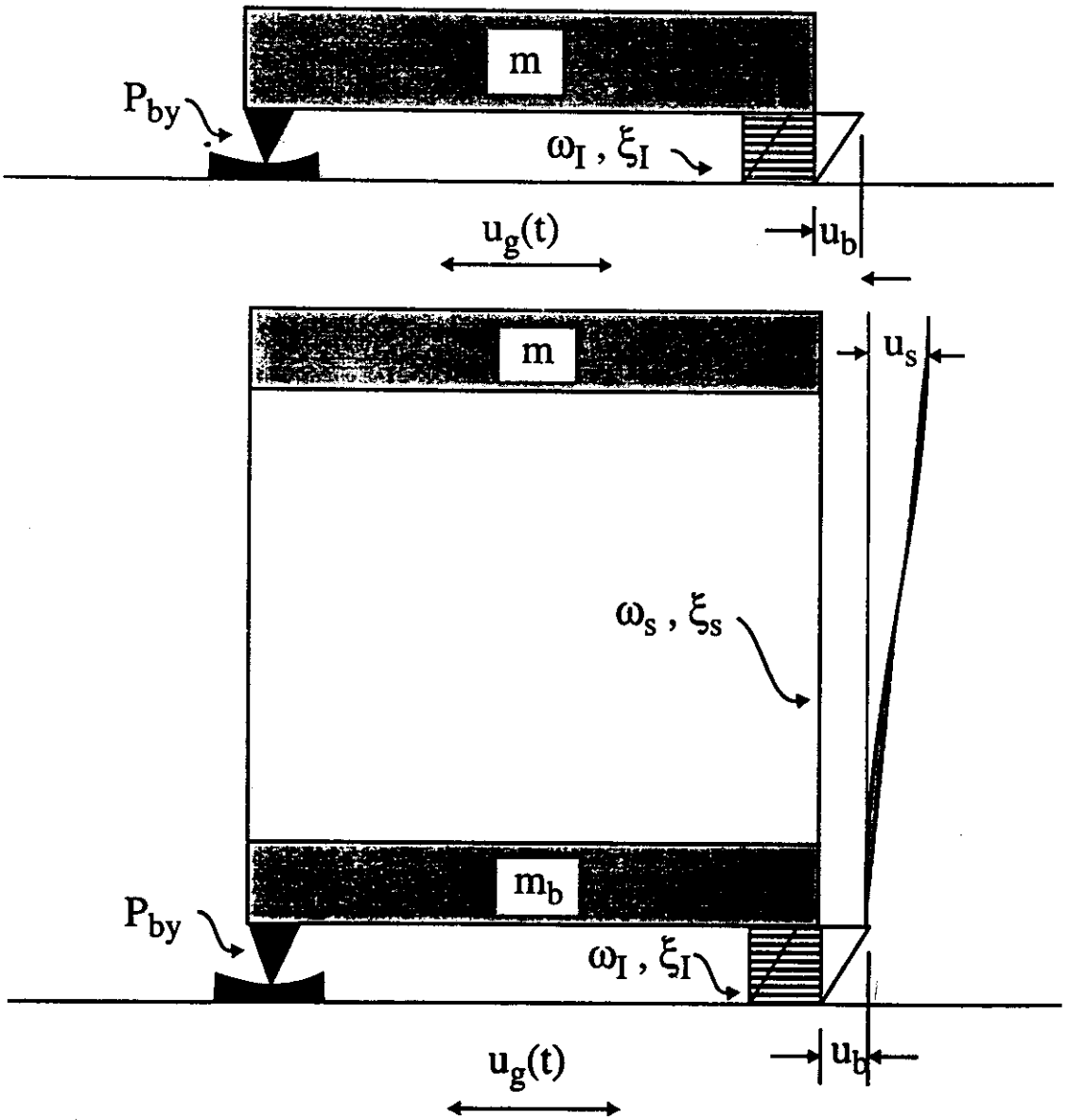

Fig. 1 Schematic of an isolated rigid block (top)
and of a two degree of freedom isolated structure (bottom)

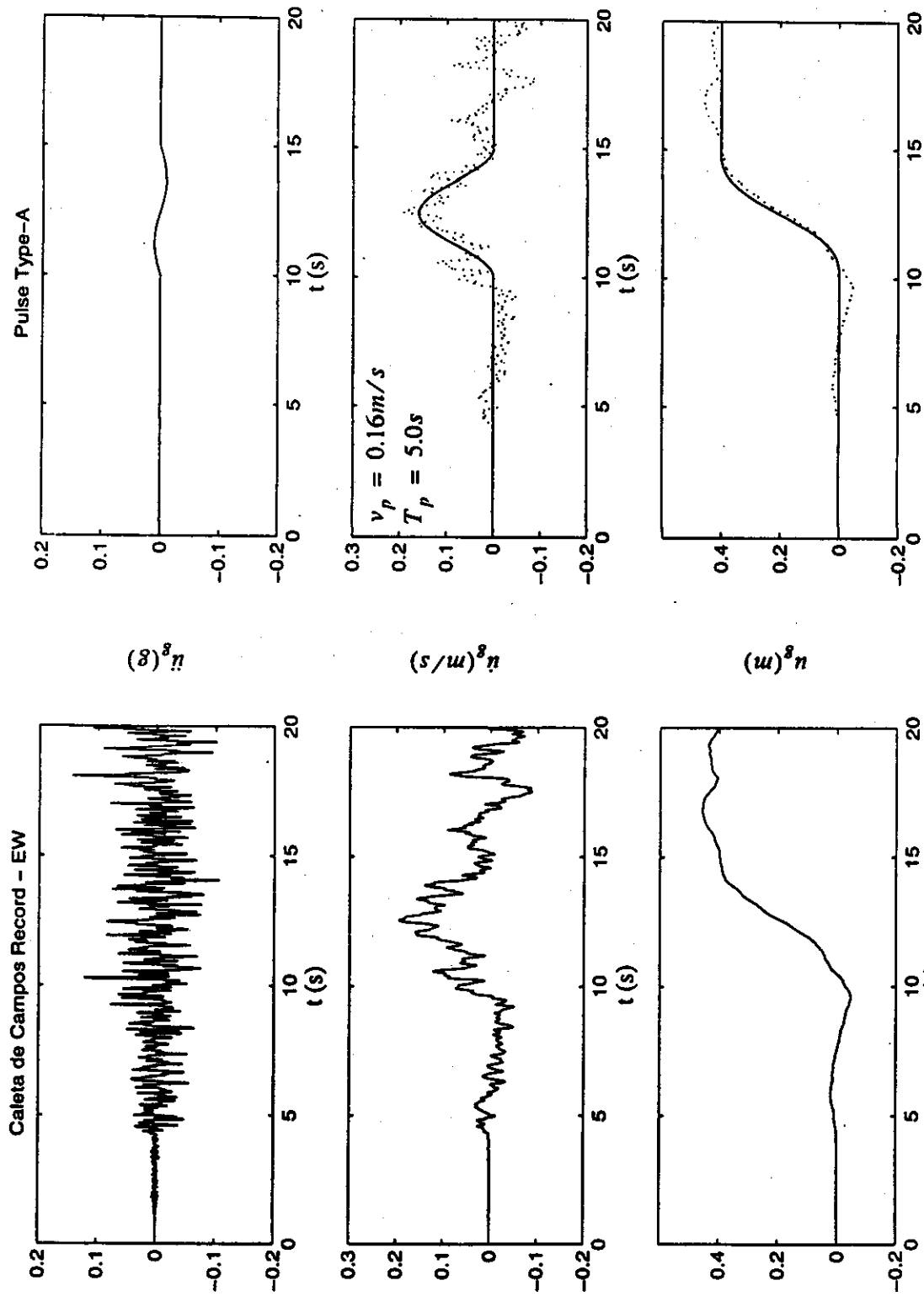

Fig. 2 Fault normal components of the acceleration, velocity and displacement time histories recorded at the Caleta de Campos station during the September 19th, 1985 Michoacan earthquake (left), and a cycloidal type A pulse (right)

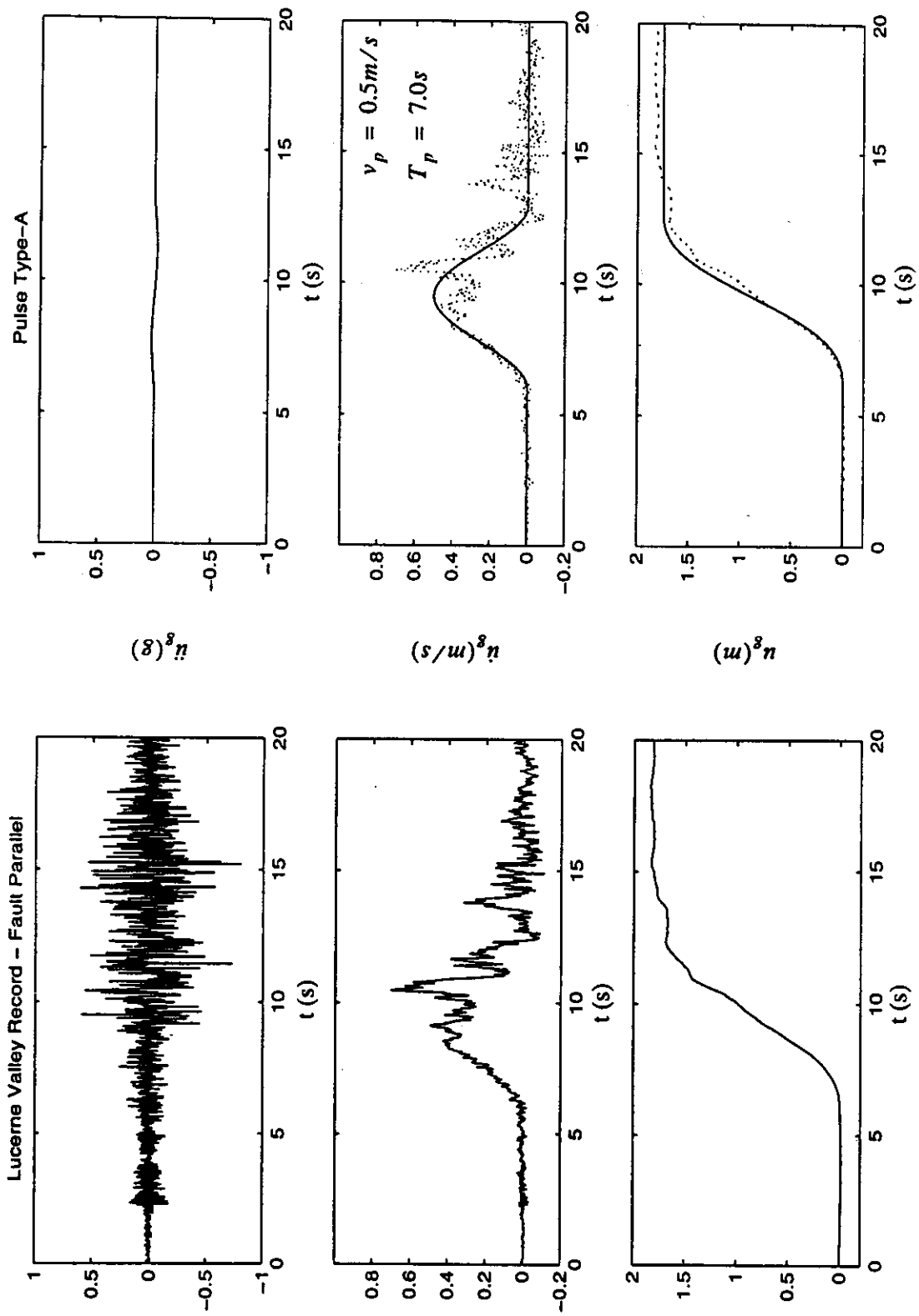

Fig. 3 Fault parallel components of the acceleration, velocity and displacement time histories recorded at the Lucerne Valley station during the June 28th, 1992 Landers, California earthquake (left), and a cycloidal type-*A* pulse (right)

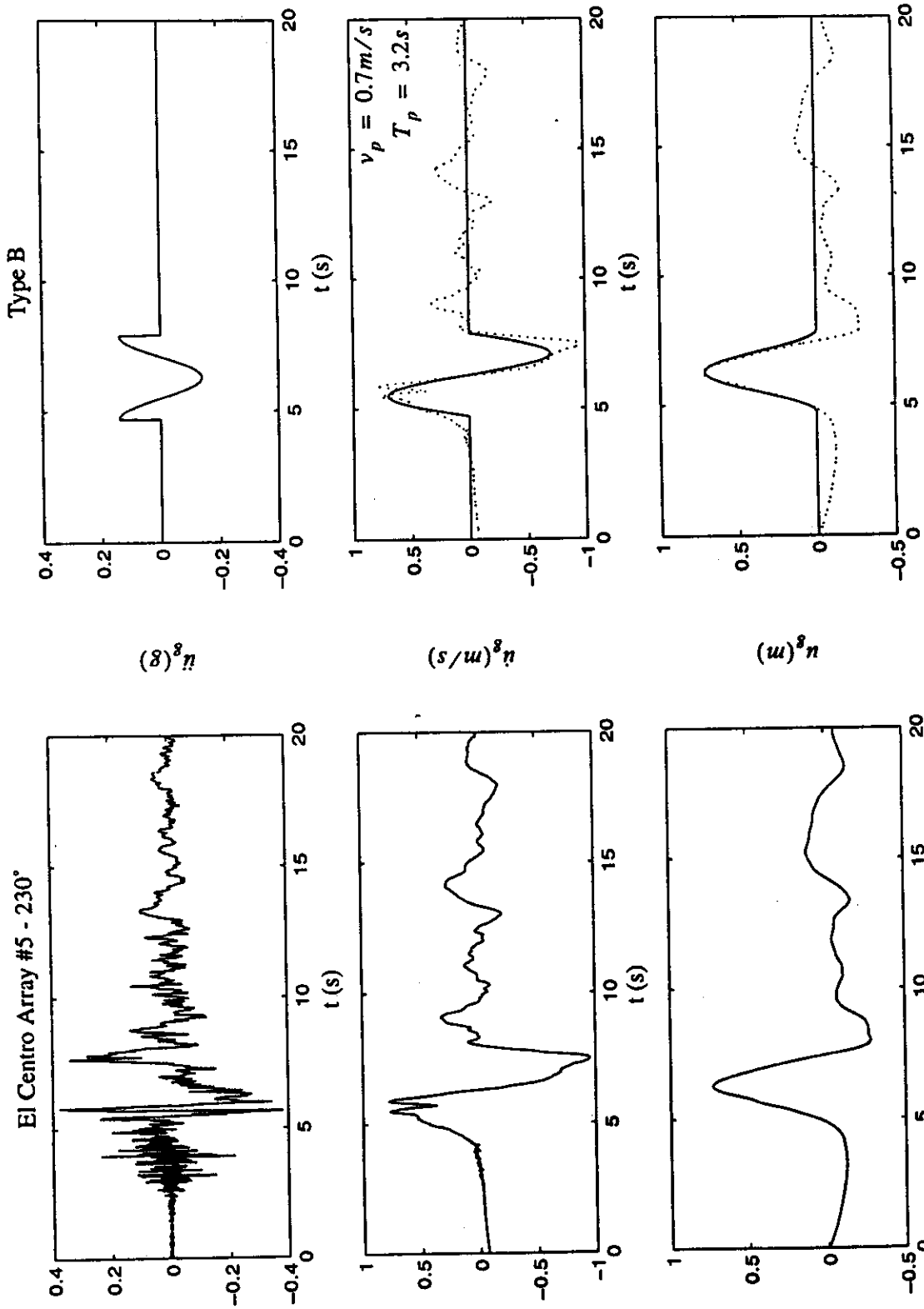

Fig. 4 Fault normal components of the acceleration, velocity and displacement time histories recorded at the El Centro Array #5 station during the October 15th, 1979 Imperial Valley California earthquake (left), and a cycloidal type-*B* pulse (right)

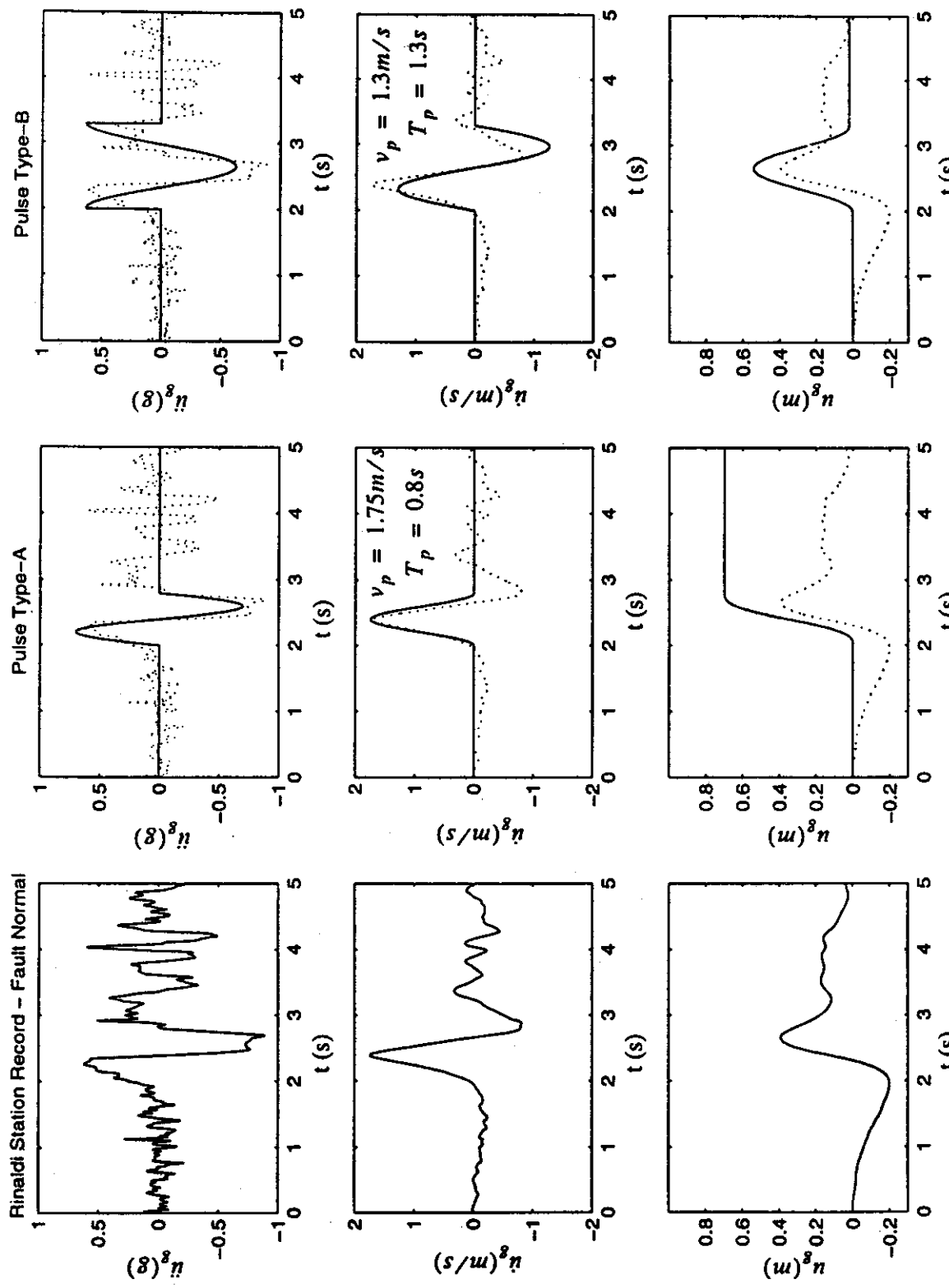

Fig. 5 Fault normal components of the acceleration, velocity and displacement time histories recorded at the Rinaldi station during the January 17th, 1994 Northridge, California earthquake (left), a cycloidal type-*A* pulse (center) and a cycloidal type-*B* pulse (right)

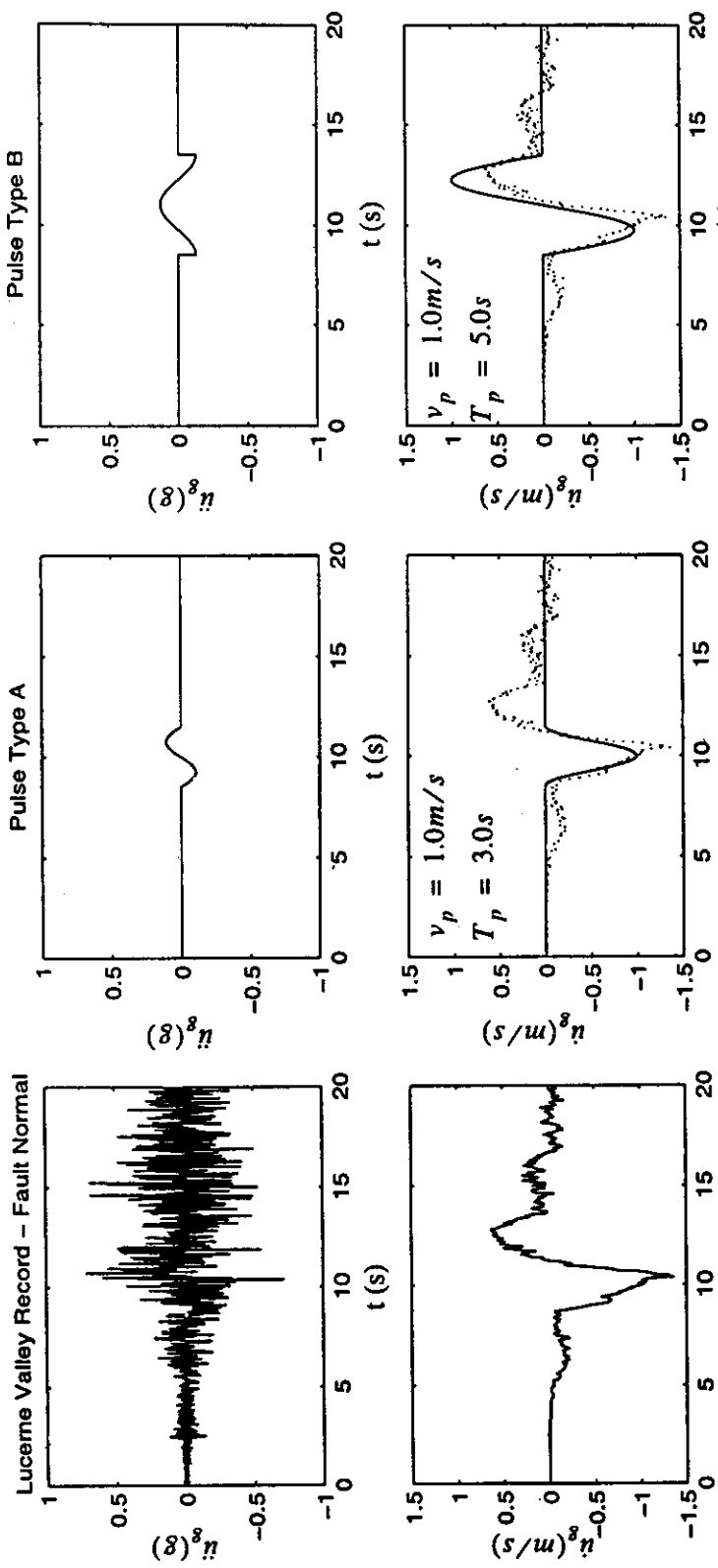

Fig. 6 Fault normal components of the acceleration, velocity and displacement time histories recorded at the Lucerne Valley station during the June 28th, 1992 Landers, California earthquake (left), a cycloidal type-*A* pulse (center) and a cycloidal type-*B* pulse (right)

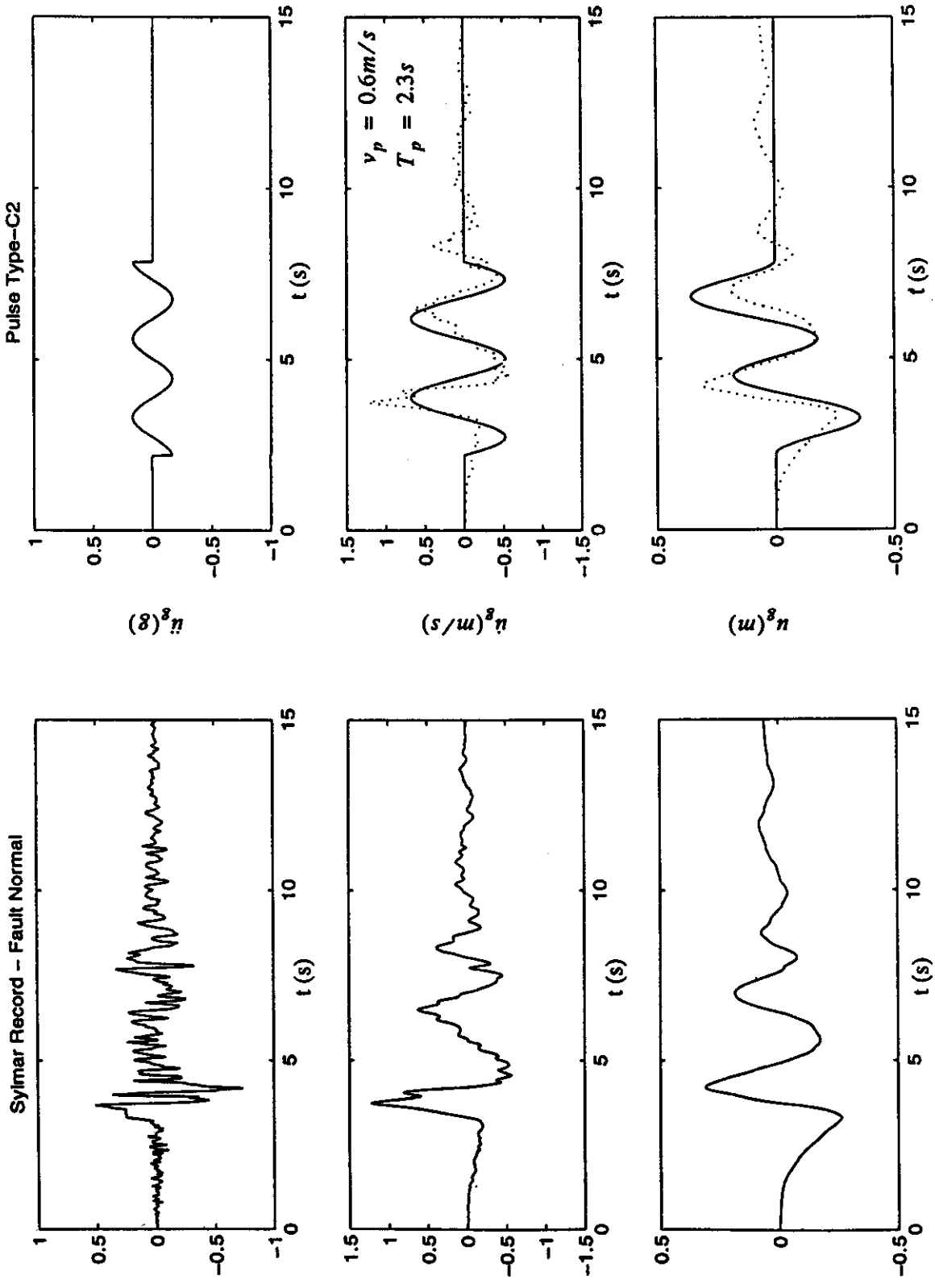

Fig. 7 Fault normal components of the acceleration, velocity and displacement time histories recorded at the Sylmar station during the January 17th, 1994 Northridge, California earthquake (left), and a cycloidal type-A type-C_2 pulse (right)

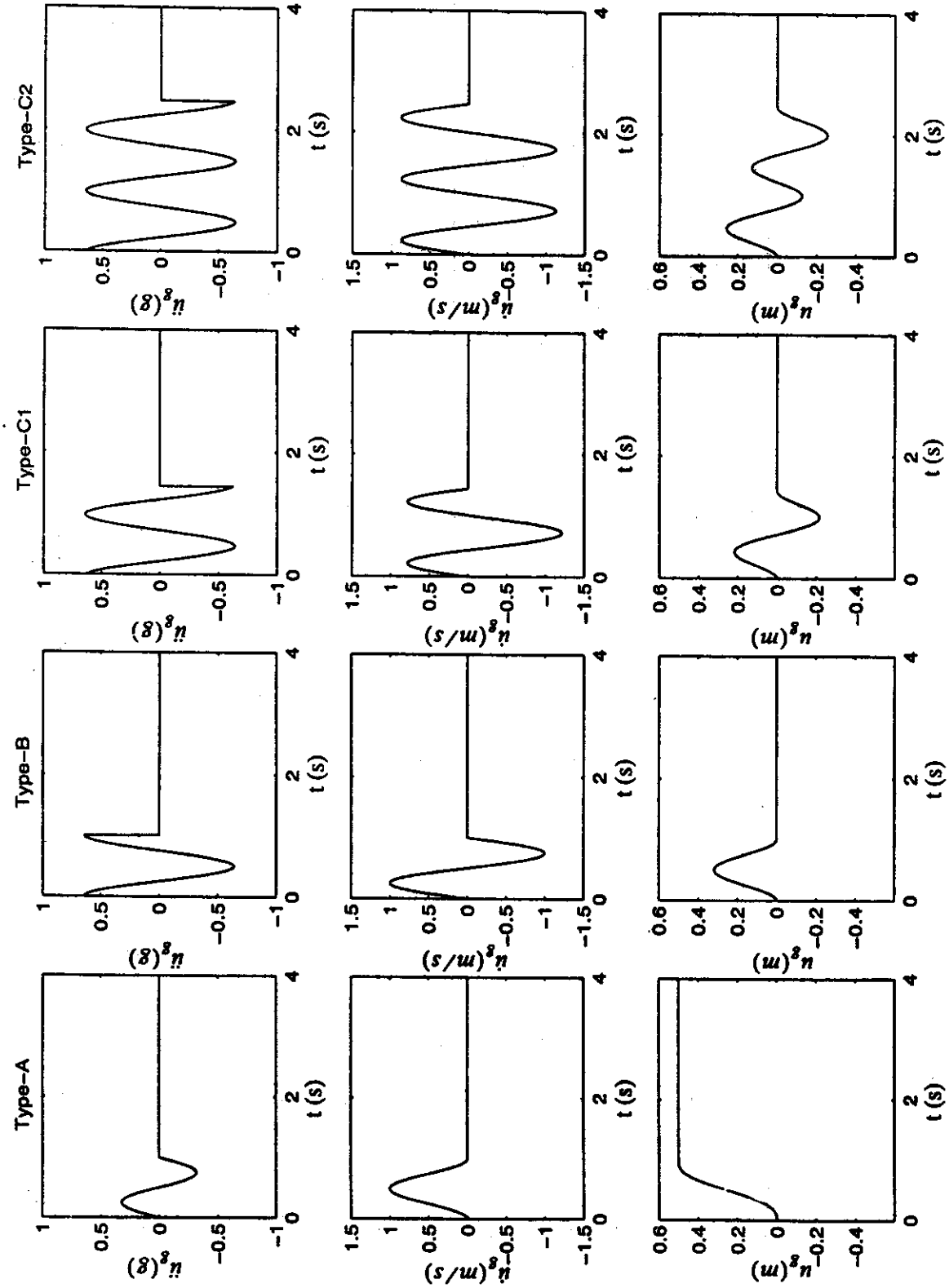

Fig. 8 Acceleration, velocity and displacement time histories of cycloidal pulses type-*A* (first column), type-*B* (second column), type-C_1 (third column) and type-C_2 (fourth column)

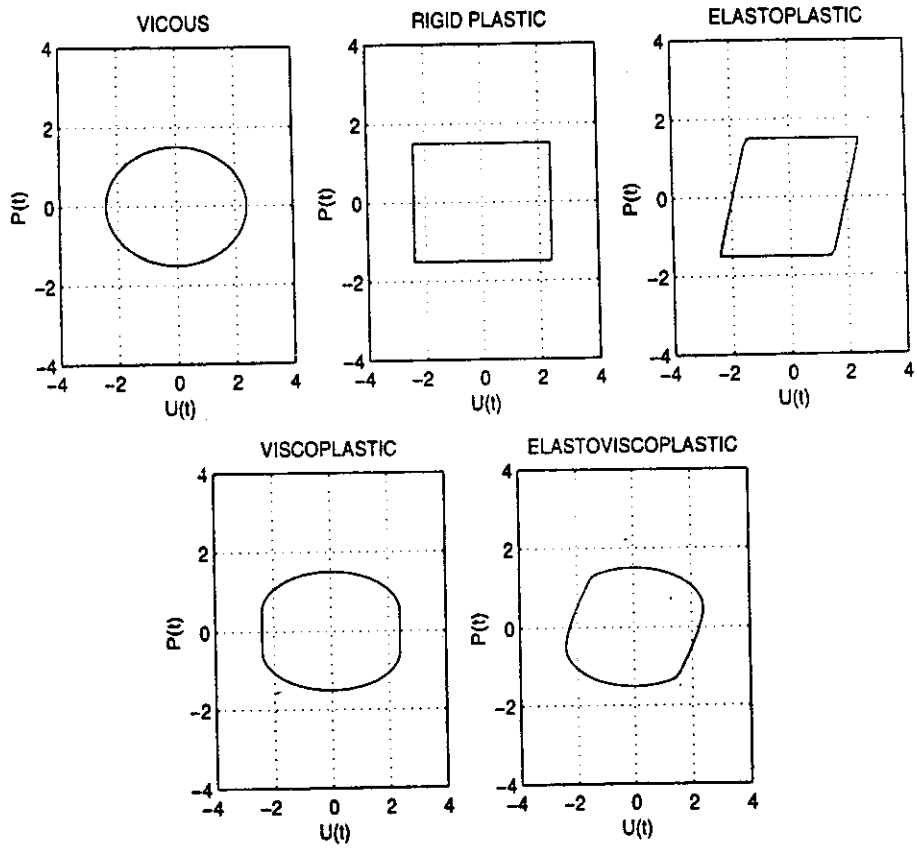

Fig. 9 Five idealizations of energy dissipation mechanisms of practical seismic isolation systems

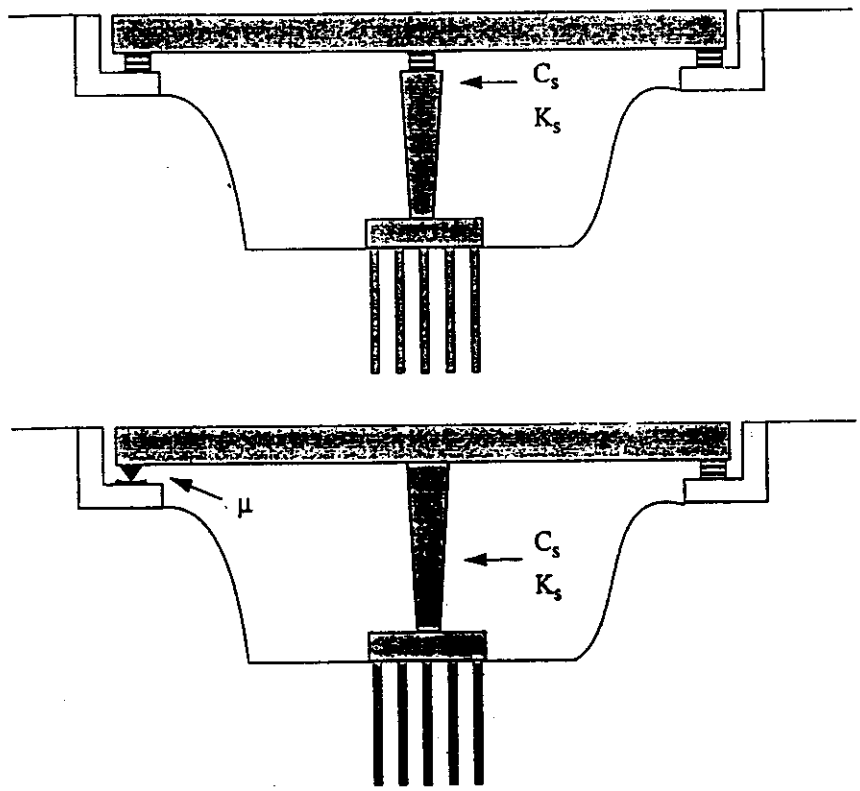

Fig. 10 Schematic of a seismic isolated overpass (top) and
of an overpass that is supported on bearings at the end abutments (bottom)

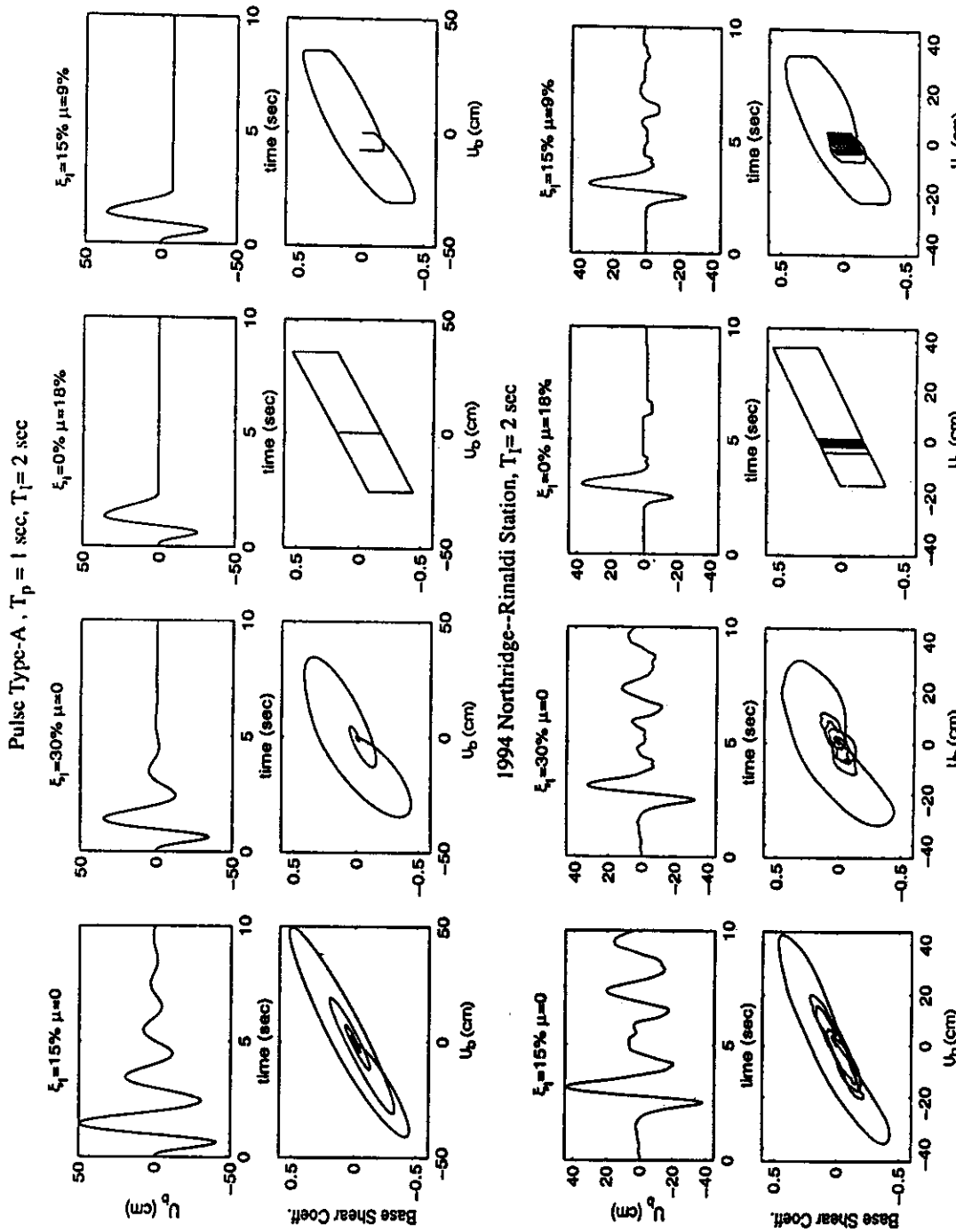

Fig. 11 Response quantities of an isolated block with T_I = 2.0 s subjected to type-*A* pulse with T_p = 1.0 s (top) and to the Rinaldi station record (bottom)

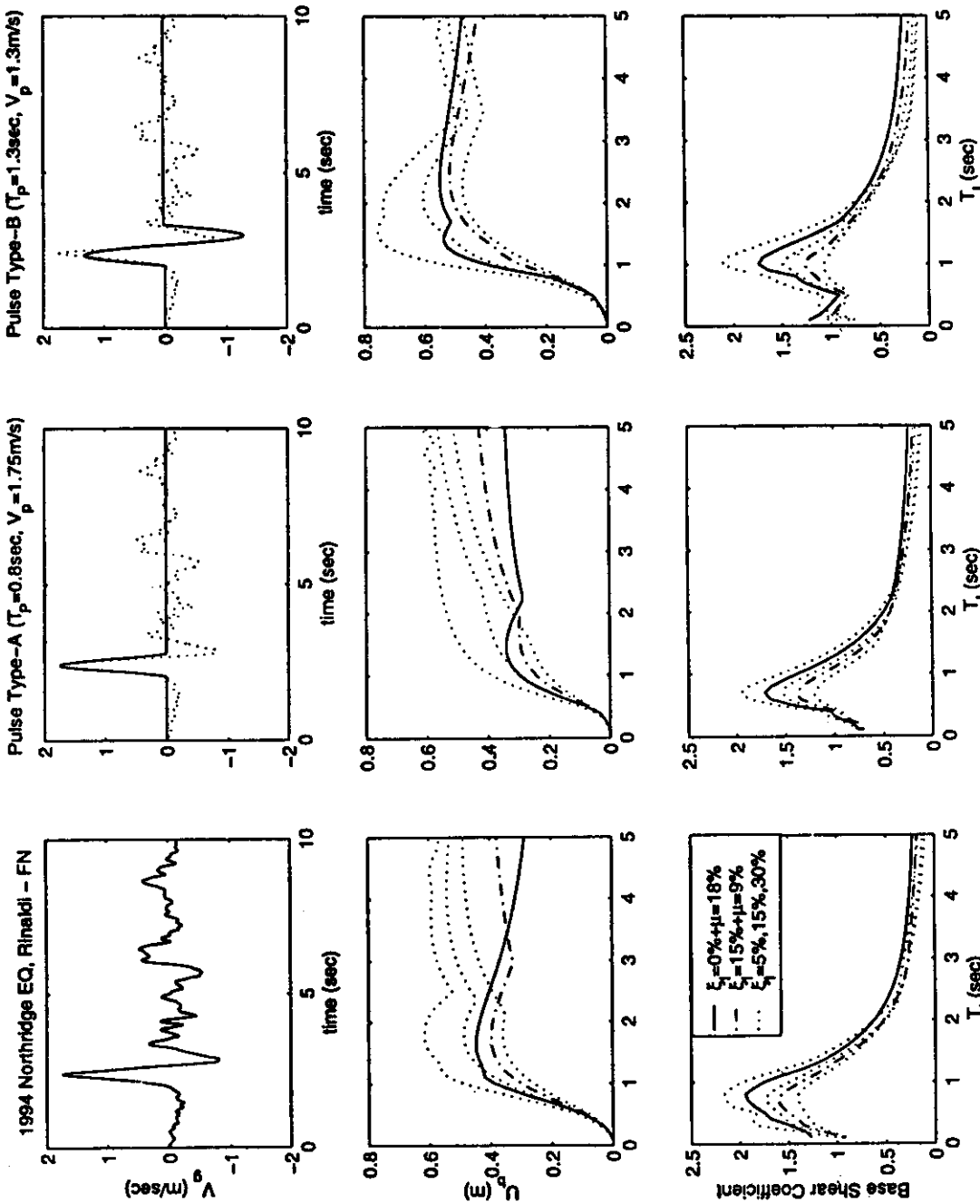

Fig. 12 Displacement and base shear spectra of an isolated block subjected to the fault normal component of Rinaldi station record (left), a type-*A* pulse (center) and a type-*B* pulse (right)

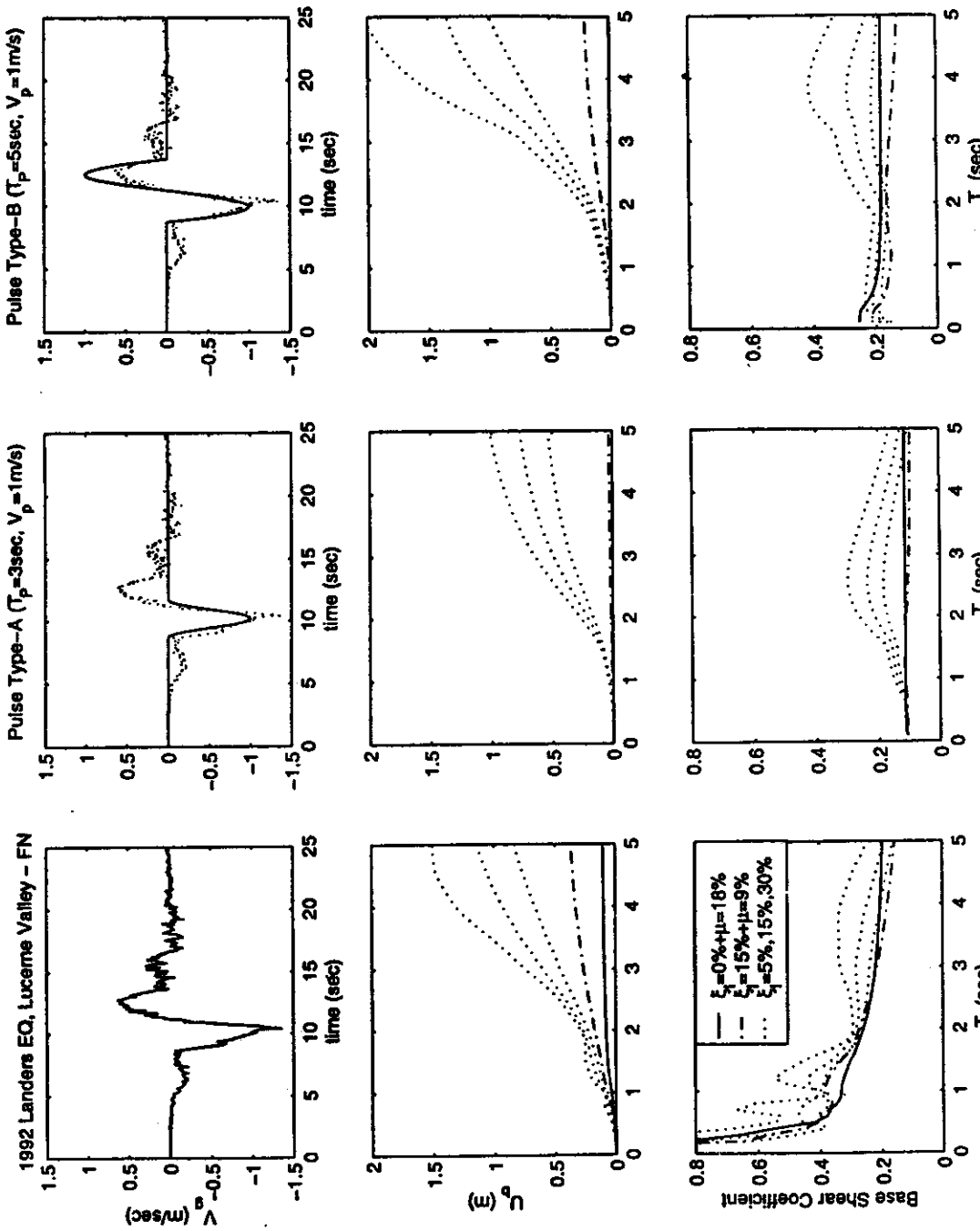

Fig. 13 Displacement and base shear spectra of an isolated block subjected to the fault normal component of Lucerne Valley record (left), a type-*A* pulse (center) and a type-*B* pulse (right)

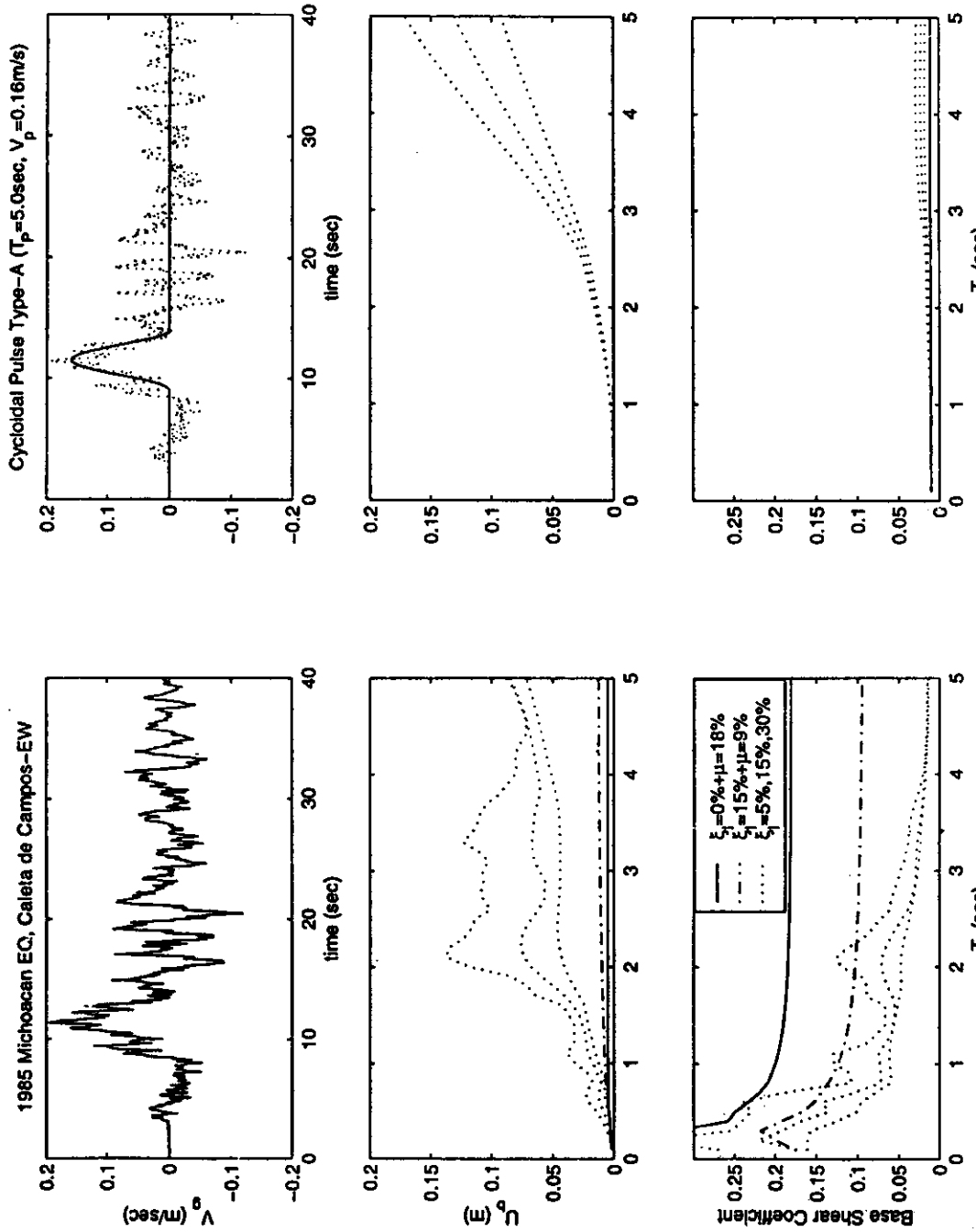

Fig. 14 Displacement and base shear spectra of an isolated block subjected to Caleta de Campos record (left) and a type-*A* pulse (right)

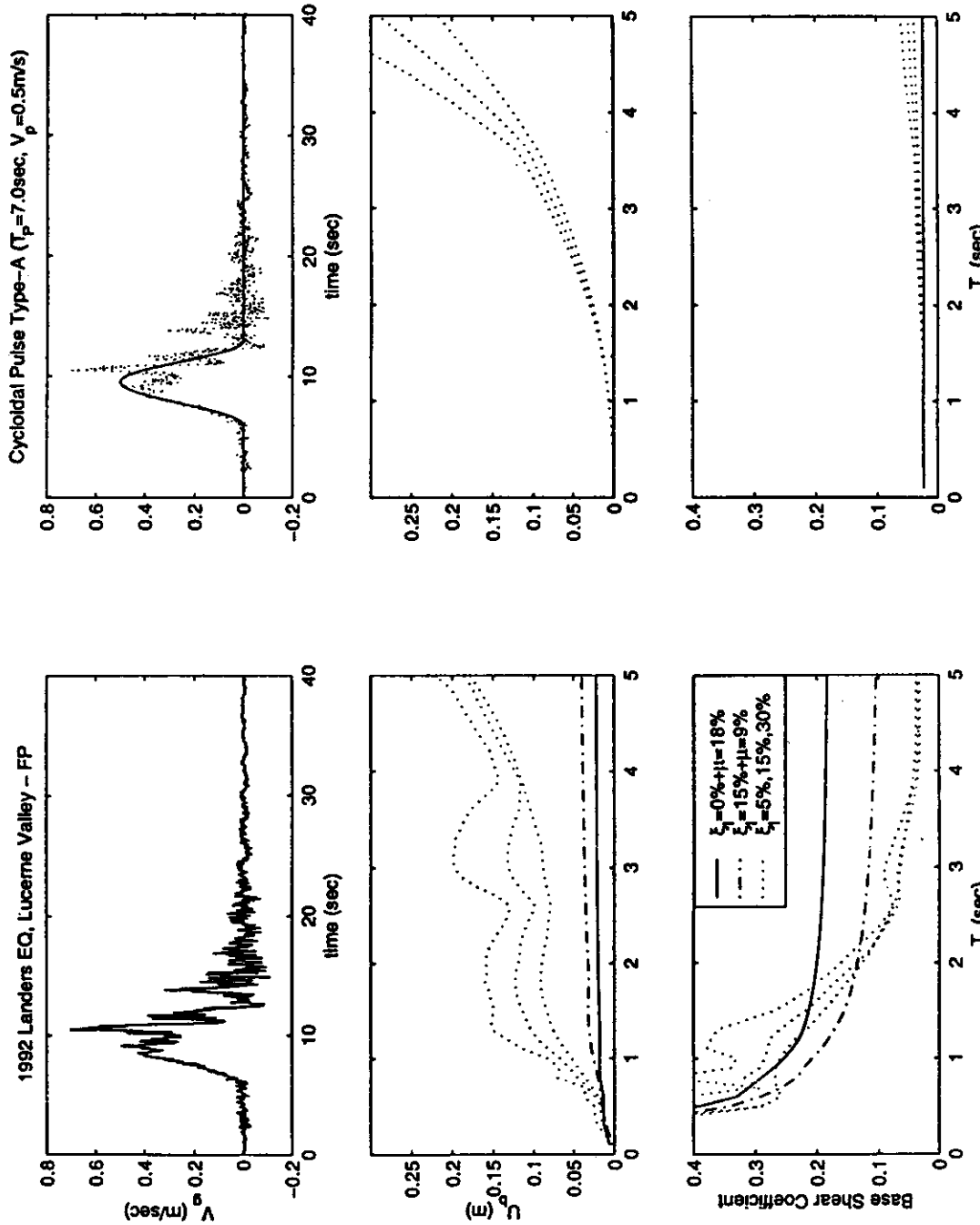

Fig.15 Displacement and base shear spectra of an isolated block subjected to fault parallel component of Lucerne Valley record (left) and a type-*A* pulse (right)

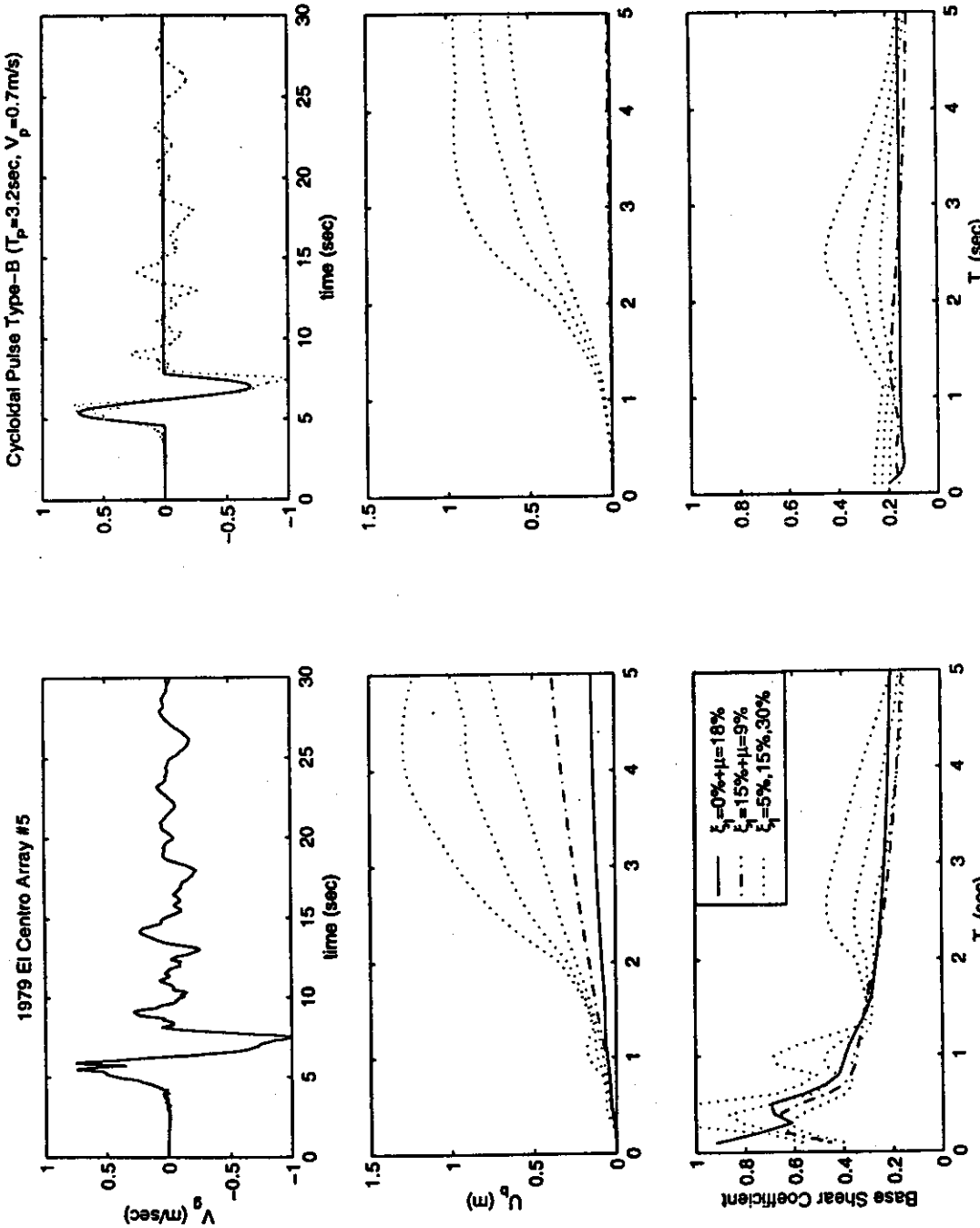

Fig.16 Displacement and base shear spectra of an isolated block subjected to El Centro Array #5 station record (left) and a type-*B* pulse (right)

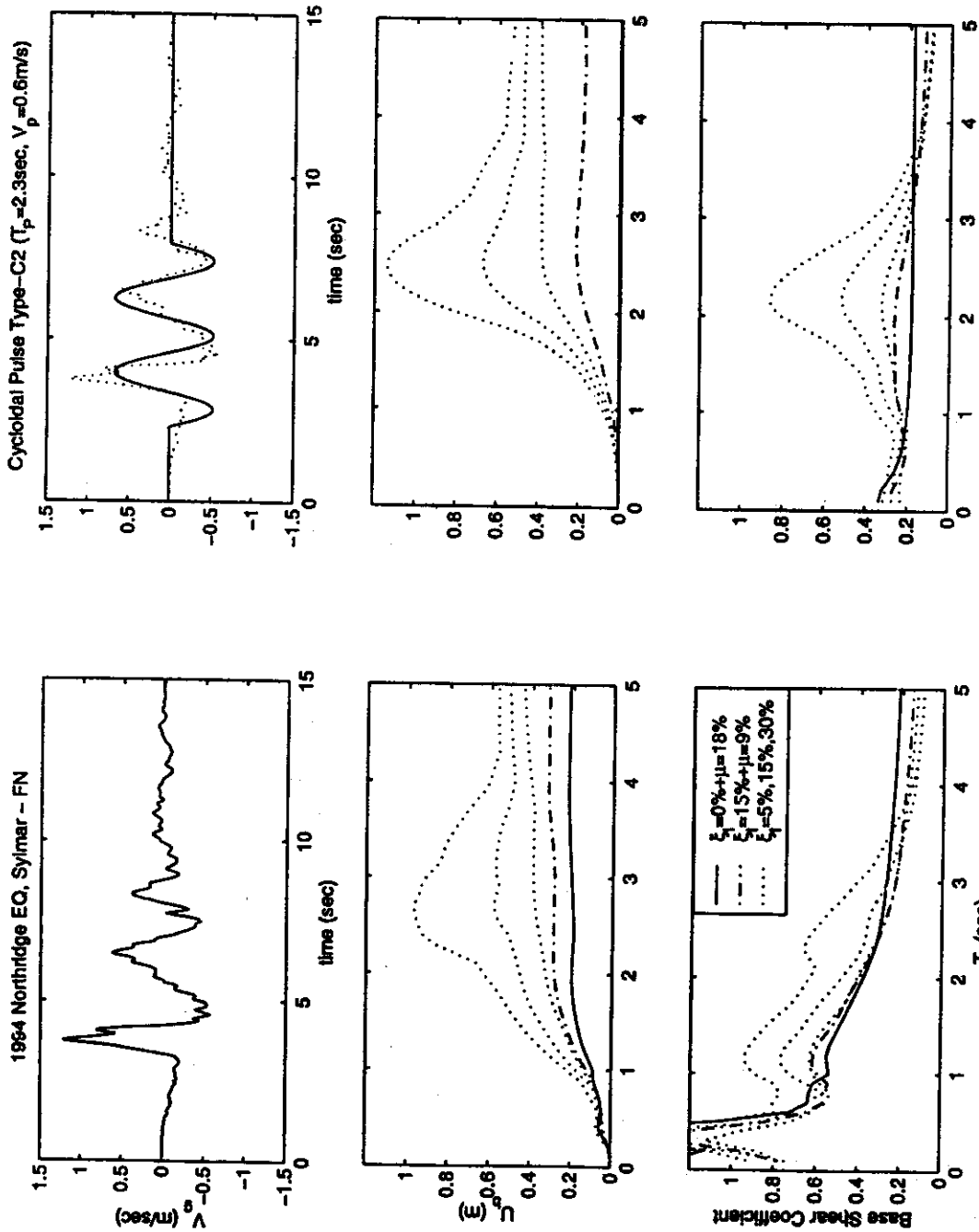

Fig. 17 Displacement and base shear spectra of an isolated block subjected to Sylmar station record (left) and a type-C_2 pulse (right)

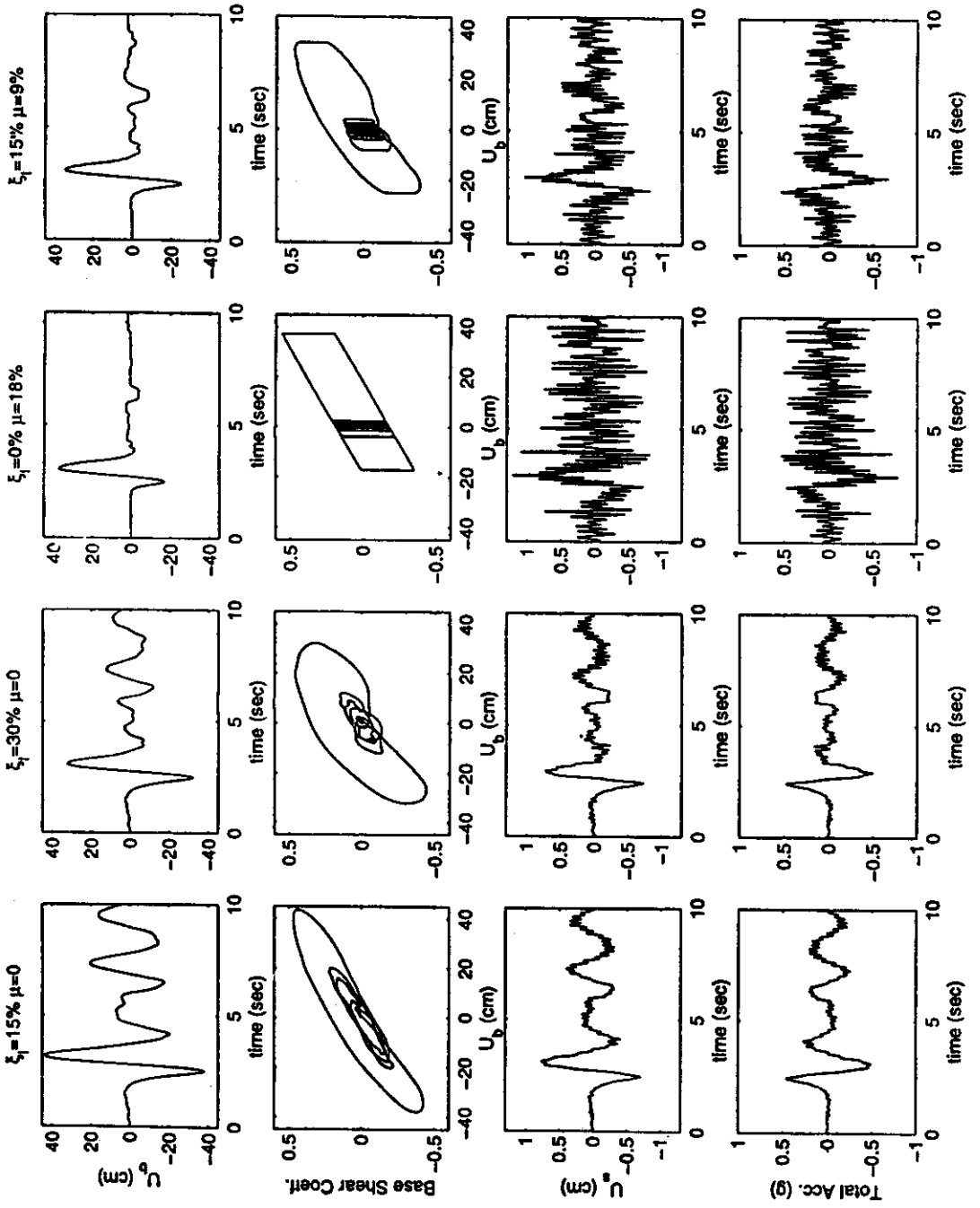

Fig. 18 Response quantities of a 2-DOF isolated structure subjected to fault normal component of the Rinaldi station record

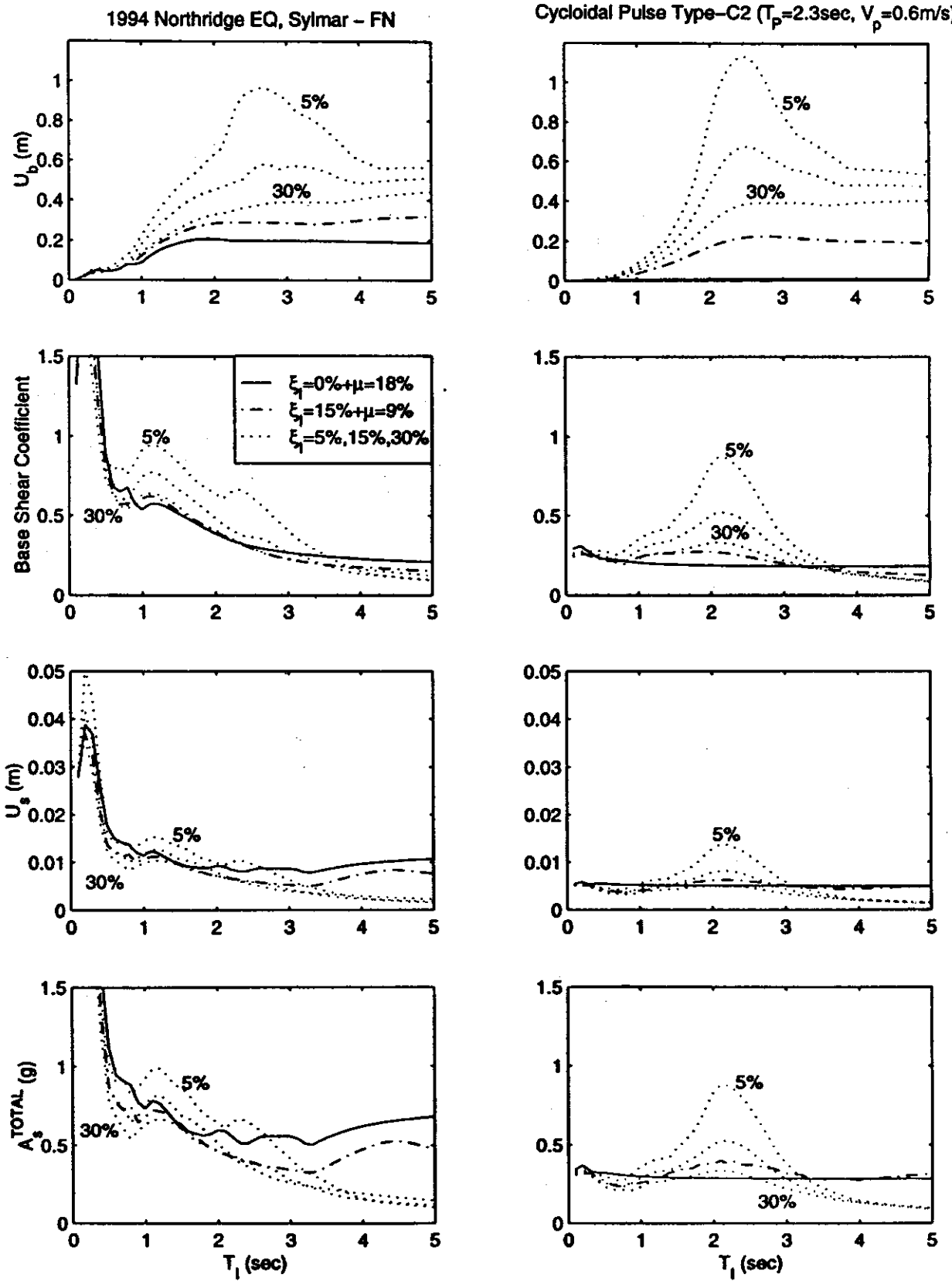

Fig. 19 Base displacement, base shear, superstructure drift and total superstructure acceleration spectra of a 2-DOF isolated structure subjected to fault normal component of Rinaldi station record (left) and a type-C_2 pulse (right)

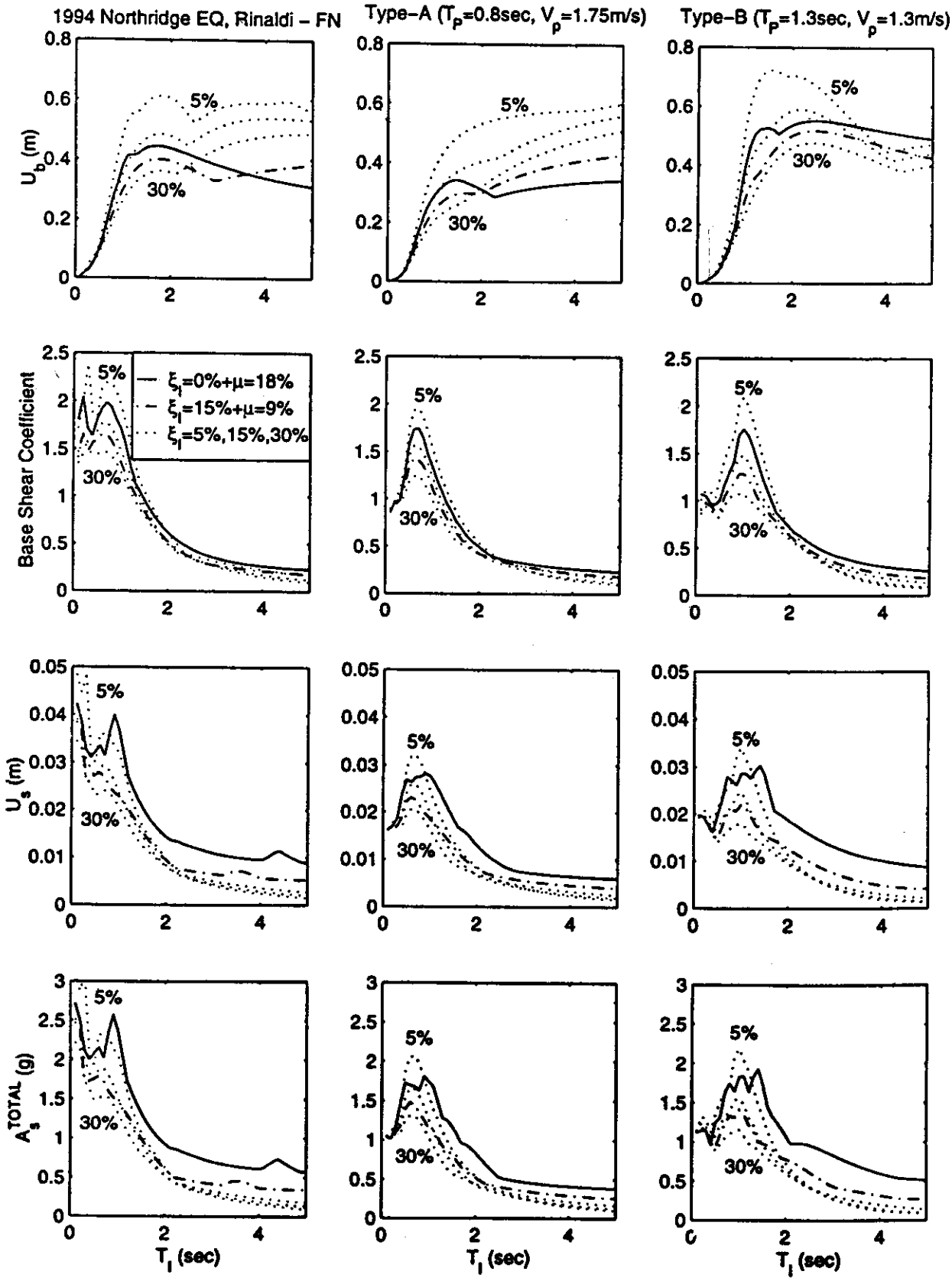

Fig. 20 Base displacement, base shear, superstructure drift and total superstructure acceleration spectra of a 2-DOF isolated structure subjected to fault normal component of Sylmar station record (left) and a type-C_2 pulse (right)